coatings

MDPI

Article

Research on the Wear State Detection and Identification Method of Huller Rollers Based on Point Cloud Data

Zhaoyun Wu *, Tao Jin, Xiaoxia Liu, Zhongwei Zhang *, Binbin Zhao, Yehao Zhang and Xuewu He

School of Mechanical & Electrical Engineering, Henan University of Technology, Zhengzhou 450001, China
* Correspondence: wuzhaoyun@haut.edu.cn (Z.W.); zzw_man@haut.edu.cn (Z.Z.)

Abstract: Throughout the huller shelling process, the rubber rollers progressively deteriorate. The velocity of the rubber rollers decreases as the distance between the rollers rises. These modifications significantly influence the rate at which rice hulling occurs. Hence, the implementation of real-time online detection is crucial for maintaining the operational efficiency of the huller. Currently, the prevailing inspection methods include manual inspection, 2D vision inspection, deep learning methods, and machine vision methods. Nevertheless, these conventional techniques lack the ability to provide detailed information about the faulty components, making it challenging to conduct comprehensive defect identification in three dimensions. To address this issue, point cloud technology has been incorporated into the overall detection of the working condition of the huller. Specifically, the Random Sample Consensus segmentation algorithm and the adaptive boundary extraction algorithm have been developed to identify abnormal wear on the rubber rollers by analyzing the point cloud data on their surface. A solution technique has been developed for the huller to compensate for the speed of the rubber rollers and calculate the mean values of their radii. Additionally, a numerical simulation algorithm is proposed to address the dynamic change in the roller spacing detection. The results show that point cloud data can be utilized to achieve real-time and precise correction of anomalous wear patterns on the surface of rubber rollers.

Keywords: huller rubber rollers; feature extraction; point cloud; numerical simulation of roller spacing

check for updates

Citation: Wu, Z.; Jin, T.; Liu, X.; Zhang, Z.; Zhao, B.; Zhang, Y.; He, X. Research on the Wear State Detection and Identification Method of Huller Rollers Based on Point Cloud Data. *Coatings* **2024**, *14*, 1209. https://doi.org/10.3390/coatings14091209

Academic Editor: Cecilia Bartuli

Received: 28 August 2024
Revised: 14 September 2024
Accepted: 18 September 2024
Published: 19 September 2024

Copyright: © 2024 by the authors. Licensee MDPI, Basel, Switzerland. This article is an open access article distributed under the terms and conditions of the Creative Commons Attribution (CC BY) license (https://creativecommons.org/licenses/by/4.0/).

1. Introduction

A huller is the machinery used to remove the outer covering of rice. Hullers can be classified into three primary categories depending on their working principles: centrifugal huller, sand disc huller, and rubber roller huller. Figure 1 illustrates a high-capacity pneumatic automatic rubber roller huller that is driven by a dual-frequency conversion motor.

The initial stage in the processing of paddy, following the cleaning process, is the separating of the hull from the inner brown rice. This procedure is popularly known as hulling [1]. The rubber roller huller operates by utilizing a pair of rubber rollers that rotate at different speeds in opposite directions. This motion applies pressure and friction to the rice grain, resulting in the removal of the hull [2]. The procedure depicted in Figure 2 illustrates a scenario where the linear speed of the fixed roller v_1 is higher than that of the movable roller v_2. Assume that a single layer of rice grains falls into the working area between two rubber rollers, as shown in Figure 2a. When the grain reaches the starting point of the rollers, its speed is lower than that of the rollers. Due to the friction between the grain and the rollers, the grain is accelerated. The two rubber rollers slide against each other, causing the grain to continue moving forward. As the grain is rolled by the rollers, the friction causes its speed to quickly reach the speed of the slower roller, while the faster roller continues to accelerate. This creates a shear force on the grain between the two rubber rollers [3]. As the fixed roller moves closer to the grain, the pressure on the grain increases, causing the shear force to grow. Once the shear force is strong enough, it tears open the rice husk, as shown in Figure 2b. This happens because the friction coefficient between the rice

husk and the rubber roller is higher than the internal friction coefficient between the rice and the rice husk. As a result, the rice husk on the side of the movable roller remains static while the rice husk on the side of the fixed roller also remains static. As the grain moves forward, it initially detaches from the rice husk on the movable roller side, followed by the brown rice grain making contact with the movable roller. The brown rice then accelerates and quickly surpasses the speed at which the fixed roller contacts the rice husk. This causes the brown rice to separate from the hull [4], completing the dehulling process, as shown in Figure 2c.

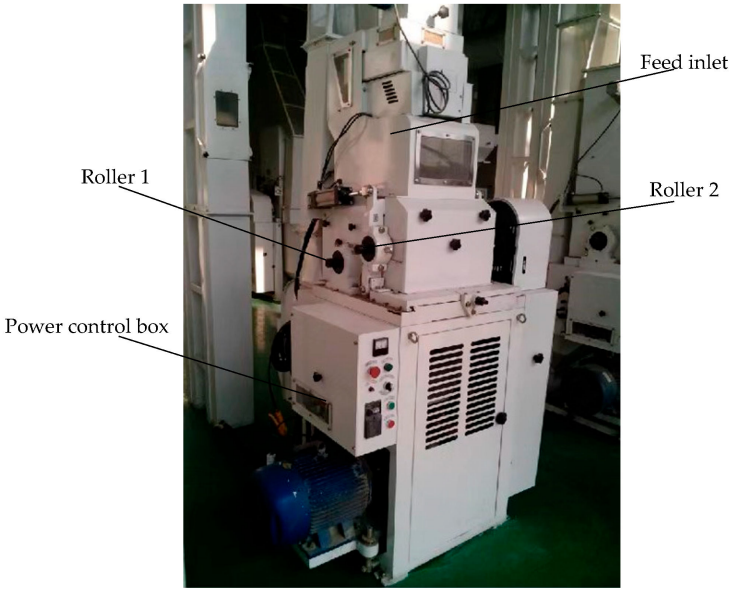

Figure 1. Large pneumatic automatic rubber roller huller.

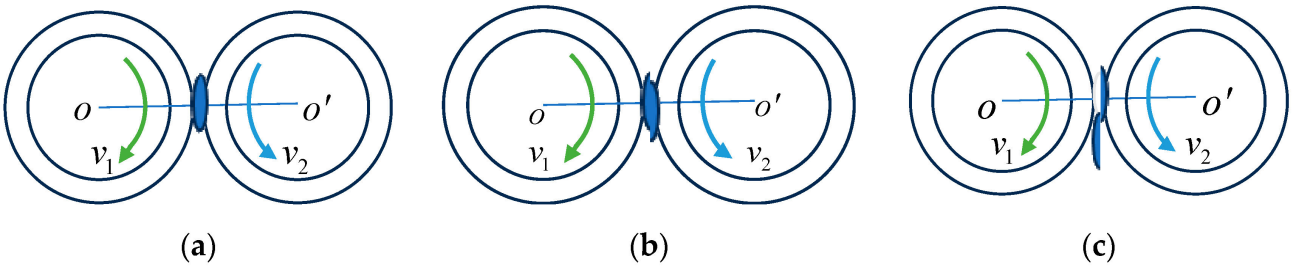

Figure 2. Rubber roller working principle diagram: (**a**) Grain contact with rubber rollers; (**b**) maximum shear force on paddy from rubber rollers; (**c**) separation of rice grains from rice husk. *O*: fixed roller center; *O*′: movable roller center; v_1: fixed roller speed; v_2: movable roller speed.

Over a prolonged duration, the rubber rollers employed in the hulling machine undergo progressive deterioration, leading to a decrease in their diameter. This leads to many issues such as a decrease in the linear velocity of the rubber roller, an increase in the distance between the rollers, a decrease in the force applied between the rollers, and an increase in the quantity of rubber utilization [5]. These factors collectively lead to a substantial decrease in the rate of paddy hulling and have a detrimental effect on the overall efficiency of the hulling machine. Therefore, it is crucial to optimize the motor speed in order to maximize the linear velocity of the rubber roller surface, precisely change the location of the movable roller to reduce the space between the rollers, and regulate the cylinder pressure to boost the pressure between the rollers. These steps guarantee the stable operation of the huller. Therefore, it is crucial to consistently observe the overall operational state of the rubber roller [6].

A commonly used method to solve this problem is removing the rubber rollers, grinding them to a specified size, fixing them, and then, reinstalling them in the mill. However, this method is restricted to conducting sporadic examinations on the rubber rollers, and the length of repairs is set and totally reliant on the experience of the workers. Therefore, it is difficult to ascertain the present operational condition of the rubber roller. The motor speed, dynamic roller position, cylinder pressure adjustment timing, and adjustment range are set exclusively by empirical knowledge, due to the absence of a precise and efficient framework. Properly calibrating the rubber roller necessitates a substantial time investment [7]. It is crucial to explore methods to manipulate the defect depth data in order to optimize the operational state of hullers. Hence, the objective of this work is to create a real-time online monitoring system that utilizes point cloud technology and sophisticated algorithms to automatically monitor the deterioration of rubber rollers, variations in diameter, and dynamics of roll spacing. This system aims to precisely regulate the motor speed and cylinder pressure, and optimize the operational parameters of the mill. The implementation of this approach enables the attainment of real-time monitoring of the roller condition of the huller, facilitating prompt maintenance and adjustment, and mitigating the uncertainty associated with depending on empirical judgment. Rani et al. [8] summarized the use of point cloud detection technology in bridges and industrial facilities in their study of defect detection using point cloud data. They paid particular attention to defect shape classification and segmentation in industrial applications, realizing that these aspects are crucial to industrial maintenance. In order to prevent waste from secondary inspection, Ntoulmperis et al. [9] examined the use of 3D forms of items for online surface defect inspection. In order to accurately determine the actual surface speed of the rubber roller by adjusting for changes in its radius, Wei et al. [10] employed a laser linear charge-coupled device (CCD) to develop an online monitoring system. This system compensates for wear by adjusting the rubber roller's surface speed in accordance with the drum's radius. This technology is capable of detecting any alterations in the radius of the rubber roller resulting from normal usage and deterioration. When the incident light is directed at an angle onto the surface of the rubber roller, the angle at which the light is reflected changes depending on the radius of the roller. By measuring the location of the reflected light, it is feasible to compute the circumference of the rubber roller and ascertain the degree of deterioration. Nevertheless, if the wear of the rubber roller is not uniformly distributed, relying merely on the position of the reflected light at a single spot may lead to an imprecise estimation of the roller's total wear. Zhang et al. [10] used a spherical grit approximation to accurately analyze the micro-cutting of grit. These researchers employed a solitary abrasive cutting model and probabilistic statistical methods to precisely calculate the rate of wear of the wheel. Jiang et al. [11] examined the rotational and unbalanced vibration of the grits to predict wear more precisely by studying the grinding contour line. Nevertheless, their investigation was restricted to evaluating the degree of wear on the rubber rollers. The surveillance level for the overall condition of the rubber roller was insufficient. Regarding the issue of adjusting the velocity of the roller surface and monitoring the gap between the rollers, in their study, Kim et al. [12] attached a non-contact displacement sensor to the top surface of the roller to measure its shape. The non-contact displacement sensor was methodically shifted at consistent intervals along the roller axis, and measurements were documented at 25 designated locations. Eddy current sensors were used to measure the shape of the rollers, while laser displacement sensors were used to evaluate the shape of the silicone sheet rollers. Furthermore, a proposal was put forward to assess the form of the rollers by installing non-contact displacement sensors on the top surface of each roller. The shapes of the two rollers were established by rotating them from any initial position in the assembly setup. The inflection point of the distance variance between the two rollers was determined using the measured form of the rollers. By adjusting the beginning position of the rollers, the interaction between the two rollers was changed in order to reduce the unevenness of the pressure. Nevertheless, the system's ability to adapt to changes in the rollers' shape may have been limited by the sampling rate of the sensors and the speed of data processing.

Krok et al. [13] suggested the installation of a pressure sensor in the non-engaging area of the two rollers. The purpose of this sensor was to acquire data that may be used to modify the spacing between the rollers, ensuring proper alignment. Byon et al. [14] performed a study to investigate the correlation between wear and the adjustment of the roller gap (pass height). They conducted single-stand reversible pilot slot rolling experiments and rolling testing in an operational bar mill. Wear profiles with specific shapes were deliberately made on the original roller grooves, which are typically not prone to wear, in order to cause wear on the grooves. A highly accurate measurement device was developed to detect the exact degree of wear during the bar mill test. Hu et al. [15] presented a roller gap prediction model in their study, which employs a compression factor particle swarm optimization support vector machine (SVM). The roller gap models for PSO-SVM, genetic algorithm (GA) SVM, and CF-PSO-SVM regression were developed using a large amount of live data. The performance of the models was evaluated using decision coefficients, mean absolute error, and root-mean-square error. In addition, the study analyzed the roller gap compensation model using the precise predictive capabilities of CF-PSO-SVM. Integrating the CF-PSO-SVM model into an existing industrial automation system may require improvements or modifications to the system. Guo et al. [16] created a sensing probe that utilizes a distance control component to scan the roller surface in the radial direction. A successful technique was found to rectify faults and improve the performance of the detection rollers. This was accomplished by enhancements made to the optical detection component, the implementation of the moving mechanism, and the optimization of the overall work process. The accuracy of identifying cot surface faults and rice huller working morphology on two-dimensional (2D) photos has significantly improved with the introduction of deep learning. The roller's operating environment and the absence of depth information in 2D photos make it impossible to derive defect measurements from 2D images, making it difficult to use point cloud data of the roller surface for overall rice huller monitoring.

To evaluate the applicability of the current detection technology in real-world conditions, this study presents a method for the real-time detection and identification of the wear status of rubber rollers using point cloud processing technologies on-site. The technique basically involves controlling the speed of the motor, detecting the operational condition of the rubber rollers, and monitoring the dynamic variations in the space between the rollers. The installation technique entails using a laser ranging sensor to obtain a three-dimensional point cloud on the surface of the rubber roller of the huller. The determination of the operational condition of the huller's rubber roller is accomplished by the analysis of a three-dimensional point cloud. The process involves the utilization of a random sampling consistency segmentation algorithm and a normal-based adaptive boundary extraction algorithm. The objective is to observe and track any atypical deterioration in the rubber roller of the huller. The radius-mean solution algorithm is utilized to calculate the extent of wear on the rubber rollers of the huller, which provides the basis for adjusting the speed of the rubber roller surface. A computational approach is devised to model the dynamic variation of the rubber roller gap. Moreover, the effectiveness of the detection concept and error compensation approach was verified through a number of experiments performed under simulated working conditions.

2. Materials and Methods

2.1. Point Cloud Data Acquisition

The identification of huller roller wear through the analysis of raw data acquired from scanning entails various distinct procedures, as depicted in Figure 3. Initially, the point cloud representing the surface of the rubber roller is obtained. Due to the influence of the instrument, the surrounding environment, and the features of the scanned target, it is inevitable that some noise will be present in the point cloud data. Therefore, the second stage involves the process of denoising the point cloud [17]. Next, the anomalous wear

imperfections in the filtered point cloud are detected. The three-dimensional point cloud data are utilized in the last stage to perceive the aberrant morphology of the rubber rollers.

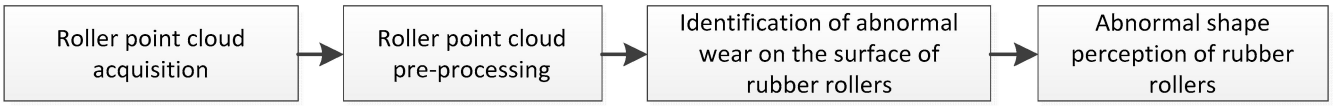

Figure 3. Technology roadmap.

2.1.1. Detection Device Design

Laser technology has spurred laser ranging research and rapid advancement. The distance to a specific point on the target item can be measured using a single laser ranging technique [18]. If the distance and positional data for each point on a target item are gathered, the point cloud can be reassembled. The spatial shape profile of the target object is shown by this point cloud. Lasers, receivers, and power supplies make up the laser rangefinder [19]. Laser distance measuring uses a pulsed laser to target an item. Meanwhile, a timer or counter starts and laser pulses or beams are sent to the object. The total time for laser pulses to reach the target and return to the receiver is recorded. The distance is computed using the laser pulse wavelength and phase. This technique can be enhanced for precision and ease. A laser transmitter, power source, transmitter optics, receiver optics, and counter make up the highly developed laser distance measurement technique [20]. The first step in calculating distance is aligning the aim. After turning on the power supply, the transmitter laser activates, sending a laser pulse signal to the target using the laser transmitter system. The counter receives a synchronization signal to start counting together with the laser pulse signal. The oscillator continuously transmits clock pulses to the counter. Laser pulses pass through the atmosphere, reach the target, then return [21]. The receiving optics system's photoelectric detector provides a pulse signal to the counter, ending counting. The counter stops counting. Laser ranging calculates distance by examining the amount of clock frequency pulses, the laser pulse wavelength, and other information throughout the counter's opening and closing phase [22]. Figure 4 depicts this procedure schematically.

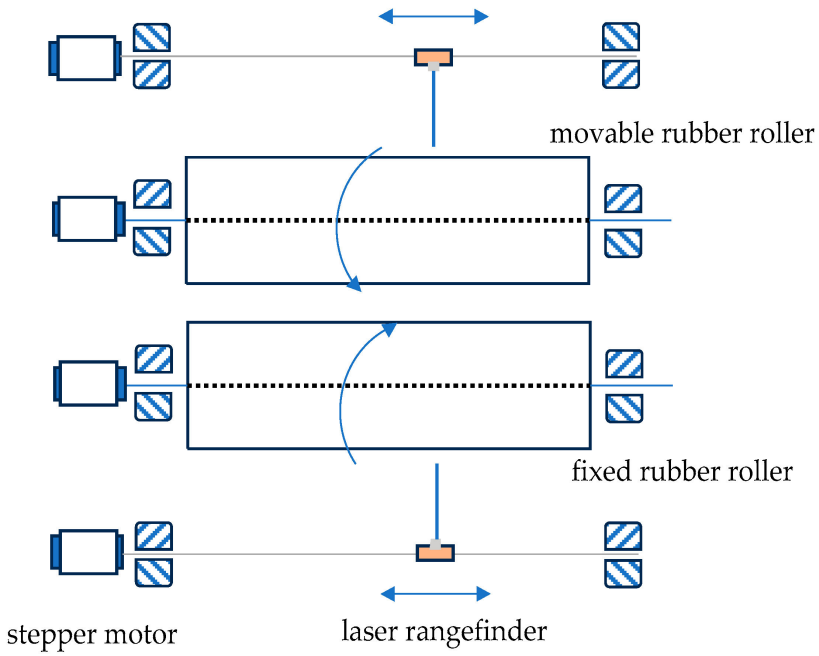

Figure 4. Laser distance sensor working diagram.

When measuring a target, the goal is to obtain a point cloud of the target within a scanning range. This is achieved by using a scanning control device to control the direction of laser emission. Each laser measurement is executed while the rubber roller rotates uniformly. This enables the calculation of distance values for specific pixels. By comparing the size of the rubber roller in the axial and time dimensions, it is possible to determine the spatial position of a specific point on the target object. By utilizing the advanced atomic STM32F103RCT6 microcontroller, the scanning device achieves exact control over the stepper motor for accurate axial order control. This allows for the repetition of laser ranging at each point in the scanning area, resulting in the complete acquisition of the point cloud of the target item. Figure 5 depicts a schematic diagram of the laser point cloud acquisition path in this work.

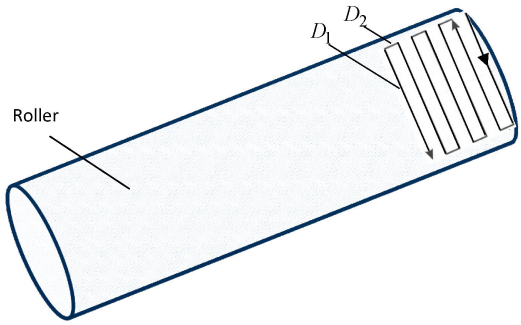

Figure 5. Schematic diagram of the path of laser point cloud acquisition. D_1: current position point cloud data acquisition path; D_2: the distance to the next set of point cloud data.

This study presents a method for laser scanning using the phase technique to measure the target point cloud. The scanning control method employed is the "S" type, where the laser ranging sensor remains stationary in the axial direction while the rollers driven by a motor rotate uniformly. By comparing the integrated angular velocity of the rollers with time, a circle of point cloud data is obtained after D_1. The subsequent scanning commences from D_2, which is the closest position to D_1 in the subsequent row, thereby employing the "S" scanning technique.

The process of retrieving the coordinates of each point on the surface of the rubber roller can be accomplished by the following steps:

1. The rotation angle of one revolution of the rubber roller is divided into multiple smaller segments based on the total time needed for one round trip of the laser distance measuring sensor. Figure 6 depicts a schematic diagram for obtaining the point cloud on the surface of the rubber roller.
2. The radius of each point is determined by calculating the difference between the distance from the laser distance sensor to the center of the roller and the distance from the laser distance sensor to the surface of the roller.
3. The coordinates of each point are determined by calculating the rotation angle for each small segment, and then, computing the x, y, and z coordinates based on the given radius and angle.

   x coordinate: $x = r\cos(\theta)$;
   y coordinate: $y = r\sin(\theta)$;
   z coordinate: $z = 0$ (the axis is placed horizontally).

The variable r represents the radius of the axis, whereas θ is the rotation angle associated with the current segment. The point cloud data of the shaft surface are obtained by capturing and storing all the calculated coordinate points. The STM32F103RCT6 microcontroller was utilized to regulate the stepping motor, which incrementally adjusts the position of the laser ranging sensor probe along the axial direction. This facilitates the acquisition of a comprehensive dataset of the rubber roller's circumference radius at various cross-section positions throughout its entire length range.

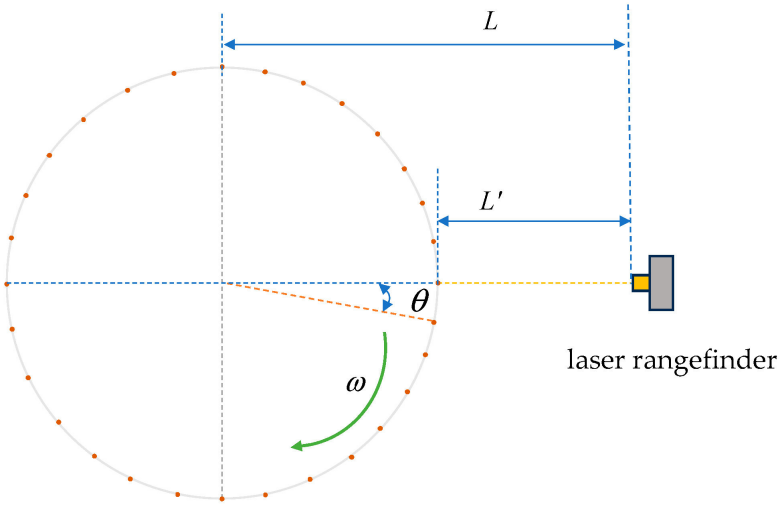

Figure 6. Schematic of point cloud data acquisition.

By following the aforementioned methods, the circular movement of the shaft can be transformed into specific points within a three-dimensional coordinate system. This allows us to gather data in the form of a point cloud, which represents the surface of the shaft. The provided data can be utilized for subsequent 3D modelling or analysis purposes.

2.1.2. Data Processing Based on Straight-Pass Filtering

Before conducting point cloud feature extraction, the acquired point cloud data should be processed [23], and the point cloud preprocessing procedure must take the unique characteristics of the point cloud into account. Initially, the backdrop of the point cloud is eliminated, followed by the application of filtering techniques to reduce noise in the point cloud. The often-employed filtering techniques include direct pass filtering, voxel filtering, statistical filtering, radius filtering, and various other algorithms [24]. Ultimately, the point cloud data are merged and streamlined to simplify the extraction of features, reconstruction of surfaces, and visualization. This enhances the efficiency of point cloud computation in subsequent stages [25].

The point cloud data may include additional object point cloud information and some noise points due to variations in device accuracy, operator expertise, and ambient conditions [17]. Hence, the obtained point cloud data inevitably include irrelevant environmental information, necessitating the elimination of pseudo-point cloud data. The acquired point cloud of the rubber roller surface is expected to have a large distribution in the X and Y ranges, but a limited range in the Z-direction. To swiftly remove outlier points in the Z-direction, a straight-pass filtering technique is employed [26].

To accomplish this, it is necessary to establish the 3D range of the point cloud and further determine whether the 3D coordinates of the point cloud fall within the established range. Only the points that fall within the range should be retained. Finally, after performing coarse processing, it may be possible to obtain the clustering of the point cloud points. The set of the original point cloud is Q_1, $Q_1 = \{q_1, q_2, q_3 \cdots q_n\}$, where n denotes the number of original data points in the point cloud; the point cloud relative to the pixel coordinates is denoted as $q_i = (x_i, y_i, z_i)$, and should satisfy the constraint

$$\begin{cases} X_{\min} \le x_i \le X_{\max} \\ Y_{\min} \le y_i \le Y_{\max} \\ Z_{\min} \le z_i \le Z_{\max} \end{cases}$$

The value range space of the obtained point cloud should be established, where $X_{\min}$, $X_{\max}$, $Y_{\min}$, $Y_{\max}$, $Z_{\min}$, and $Z_{\max}$, denote the maximum and minimum values of the

coordinates of the point cloud space. According to the coordinates of outlier points or target workpieces, the filtering range of the passthrough filter is set in order to accurately save the points that satisfy the desired coordinates.

2.2. Identification of Abnormal Wear Condition of Rubber Rollers

2.2.1. Four Common Types of Rubber Roller Wear Patterns

Various forms of wear can arise during the operational use of the huller [27]. Under regular operating conditions, the rubber rollers have a surface layer that is smooth and has a uniform thickness that decreases. As the usage period increases, it is evident that the radius of the rubber rollers in the radial direction decreases to some extent, as depicted in Figure 7a. This alteration is a typical occurrence in the operational process of the huller.

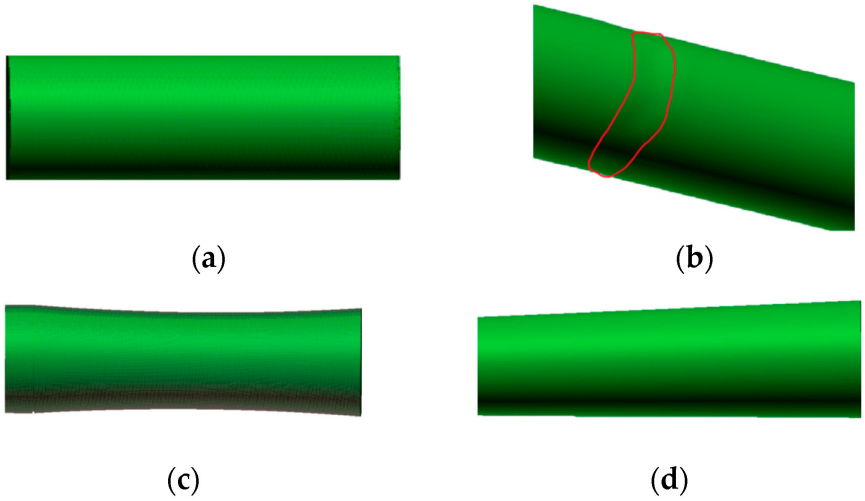

Figure 7. Four common types of rubber roller wear. (**a**) Normal wear of rubber roller; (**b**) abnormal wear I of rubber roller; (**c**) abnormal wear II of rubber roller; (**d**) abnormal wear III of rubber roller.

Abnormal wear phenomena I and II occur on the rollers when there is uneven feeding throughout the production process. The hallmark characteristics of these atypical wear patterns include wearing tracks that closely resemble the form of a bottleneck and grooves. These specific types of abnormal wear usually arise when the roller's surface encounters pressure and friction that surpasses the characteristic range at some locations. Consequently, there is a rapid decline in these focused regions [28], as shown in Figure 7b,c.

Abnormal wear phenomena III occurs when the roller is abnormally worn due to insufficient stiffness of the support system, as a result of the unequal distribution of pressure on the roller surface during operation, the removal of the roller surface material occurs in a non-uniform manner. This leads to the formation of a conical wear pattern [29], as shown in Figure 7d. The main objective of the experiments in this section is to determine the type of roll wear by utilizing an algorithm and analyzing the point cloud data of the roller surface, which is categorized into four different categories of wear. The experimental platform utilized for the experiments in this subsection consists of an Intel Core i5-5200 CPU running at a clock speed of 2.50 GHz, 4 GB of RAM, a 64-bit operating system (Windows 10), Visual Studio 2019 C++ as the programming environment, and the open-source point cloud library PCL 1.8.0. The development environment for the PCL open-source library was employed for programming in Visual Studio.

1. Abnormal wear I state identification

During rice hulling operations in rice hullers, it is common to notice aberrant wear of type I. This wear causes excessive wear of the rubber rollers in a specific location, resulting in a reduction in the diameter of those rollers in that particular area. This work utilizes a sophisticated algorithm to precisely analyze and measure the extent of wear in a certain

type of roller. The system fits a mathematical model to the external point cloud data, enabling it to reliably distinguish and identify rollers that exhibit anomalous wear. By meticulously dividing the point cloud data on the roller surface, the alterations in geometry linked to aberrant wear can be distinctly exposed.

The RANSAC (Random Sample Consensus) algorithm [30] has been extensively employed in several shape identification assignments [31]. The essence of the technique rests in executing two iterative procedures on the provided point cloud data: building a fictional model, and subsequently, validating it. Initially, hypotheses are formed by randomly selecting a minimum point dataset. From this dataset, the appropriate parameters of the shape model are estimated. While establishing the characteristics of a plane, a minimum of three points is necessary to accurately estimate the model parameters. Subsequently, the unrestrained points within the point cloud are subjected to evaluation using the potential shape model in order to determine the extent to which the model accurately represents these points. After a specific number of iterations, the algorithm determines the shape model that most accurately represents the bulk of the data points and proceeds to process the remaining data as the final outcome. This work utilizes the RANSAC algorithm to investigate and create a point cloud data processing technique that can accurately identify and separate the faulty areas of rubber rollers [32]. The method enables the precise segmentation of point sets associated with surface defects of rubber rollers from the original point cloud data. The segmentation provides essential data for subsequent analysis of wear and maintenance. Point cloud data demonstrate superior geometric properties, and mathematical models can be employed to explain the picture with greater effectiveness. Cylinders, being a fundamental geometric shape, can be precisely specified using a mathematical model. Therefore, model-based fitting approaches are commonly used to extract cylindrical surfaces. RANSAC is a widely used method that aims to gather points with similar qualities within a cylindrical surface model. The RANSAC technique is used to segment the cylindrical model from the rest of the point cloud. The RANSAC algorithm operates by randomly selecting a subset of points from the point cloud, and thereafter, attempting to fit a model in the shape of a cylinder [33]. If the model aligns with a significant number of points, it is deemed to have discovered a favorable representation of the model. The technique is iterated multiple times to enhance the likelihood of discovering the optimal model. The RANSAC algorithm yields more efficient outcomes with enhanced resilience. This technique offers more benefits in comparison to least squares fitting due to its ability to avoid fitting all the points in the point cloud, hence reducing the occurrence of significant errors. The RANSAC algorithm enhances the accuracy of the fitted model by eliminating the outliers, specifically the maximum and minimum values. Given that the rubber roller has a cylindrical surface, it is theoretically possible to extract the point cloud data from the rubber roller surface using cylindrical surface fitting. This method can be used to identify and isolate defective areas on the rubber roller surface. The application of this approach for the monitoring and prevention of wear on huller rubber rollers represents a novel and highly practical technical solution. The flow chart of the RANSAC algorithm for preprocessing roller surface point cloud data is depicted in Figure 8.

2. Identification of abnormal wear II and III defects of rubber rollers

During the operation of the huller, there were occasional instances of anomalous wear phenomena II and III on the rubber rollers. This resulted in irregular wear patterns on the surface of the rollers, such as conical shapes and bottlenecks. These wear patterns can be observed in the point cloud data of the rubber rollers, as shown in Figure 7. The predominant wear pattern seen was a bottleneck pattern, characterized by a substantial central section and comparatively thinner ends, indicating a loss of the work roller's effective straightening capability and necessitating its replacement. Furthermore, the absence of rigidity in the support structure can result in heightened deformation of the rollers, thereby increasing the likelihood of fatigue damage and reducing the lifespan of the rollers [34].

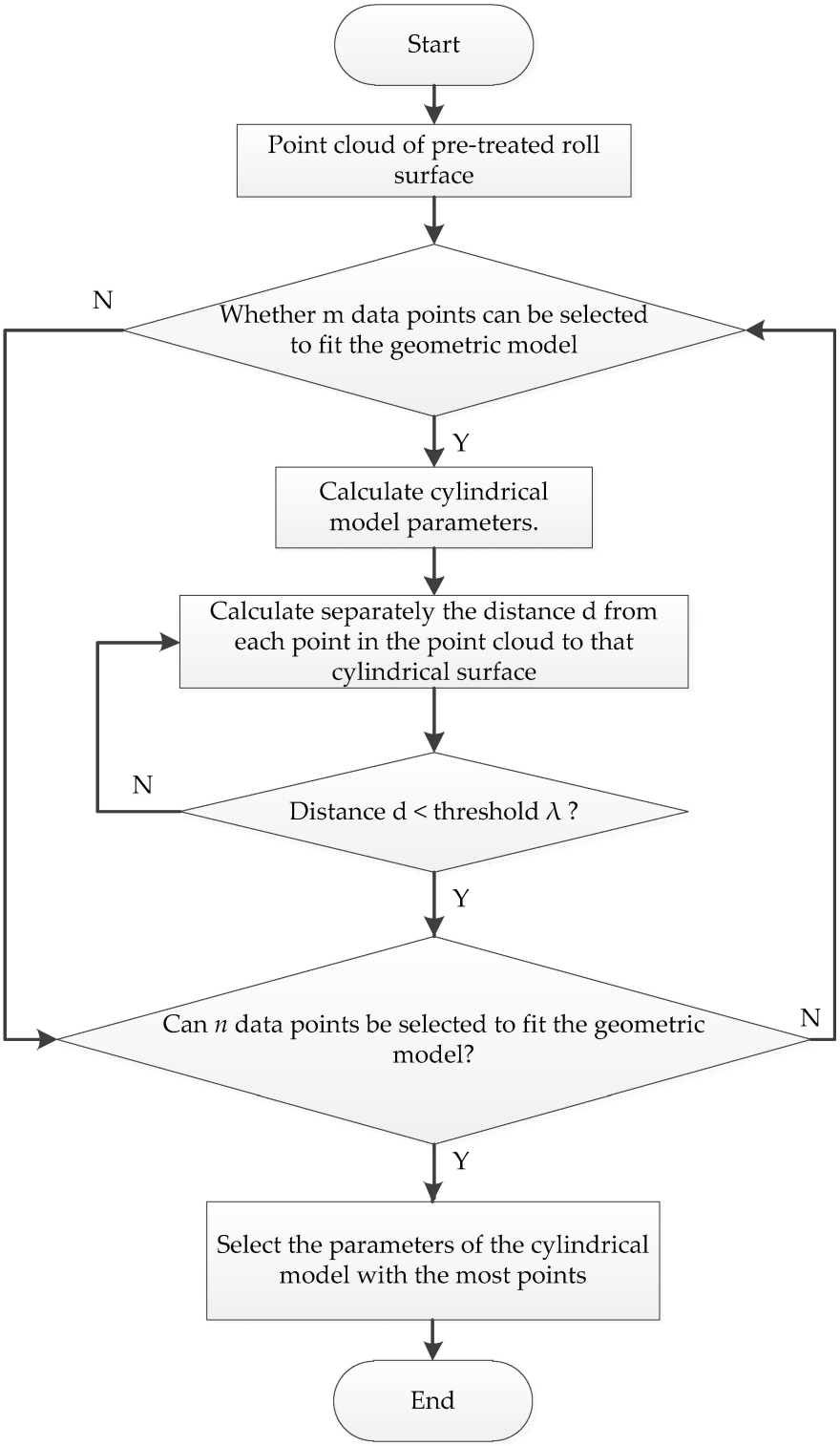

Figure 8. Flowchart of the RANSAC algorithm. Y: fulfills the requirements of the current step; N: fails to meet the constraints of the current phase.

During the regular operation of the huller, the rubber roller revolves around a stationary axis. As a result, any flaws on the surface of the rubber roller will consistently appear in the same direction along its circumference. The contour extraction method employed is derived from the angle formed by the projection vectors of the investigated point and neighboring points on the tangent plane. If a point is a boundary point, the angle between the projection vector of the point on the tangent plane and the projection vectors of the

other points is much bigger compared to the angle between the projection vectors of non-boundary points. This technology allows for the effective identification of contour edges on the surface of the rubber roller [35], providing a precise dataset for further analysis and processing. The main steps of the algorithm are as follows:

1. The least squares method was used for fitting and the equation of the fitted plane was set as

$$\begin{cases} ax + by + cz = d(d \geq 0) \\ a^2 + b^2 + c^2 = 1. \end{cases} \tag{1}$$

The distance from any point to the plane is expressed as

$$d_i = |ax + by + cz - d| \tag{2}$$

Extreme values are a precondition for locating the appropriate plane. $e = \sum_{i=1}^{n} d_i^2 \rightarrow \min$

$$f = \sum_{i=1}^{n} d_i^2 - \lambda\left(a^2 + b^2 + c^2 - 1\right) \tag{3}$$

This enables us to determine the partial derivatives of variables a, b, and c:

$$\begin{pmatrix} \sum \Delta x_i \Delta x_i & \sum \Delta x_i \Delta y_i & \sum \Delta x_i \Delta z_i \\ \sum \Delta x_i \Delta y_i & \sum \Delta y_i \Delta y_i & \sum \Delta y_i \Delta z_i \\ \sum \Delta x_i \Delta z_i & \sum \Delta y_i \Delta z_i & \sum \Delta z_i \Delta z_i \end{pmatrix} \begin{pmatrix} a \\ b \\ c \end{pmatrix} = \lambda \begin{pmatrix} a \\ b \\ c \end{pmatrix} \tag{4}$$

That is, $Ax = \lambda x$ transforms the equation into a problem of finding the eigenvalues and eigenvectors of the matrix A. The matrix A is the covariance matrix of N points. $(a, b, c)^T$ are the eigenvectors of the matrix to find the plane equation $(a, b, c)^T$ for the point (x_0, y_0, z_0).

2. Identify the perpendicular lines that intersect the plane, including the point $P_i (i = 0, 1 \cdots n)$ and the point $P_j{}'(x', y', z')(i = 0, 1 \cdots n)$. The normal vector is $PP\prime$ and the plane is $\overline{n} = (a, b, c)$. Then, the parametric equation of $PP\prime$ is

$$\begin{cases} x = x_i - at \\ y = y_i - bt \\ z = z_i - ct \end{cases} \tag{5}$$

The point $P_i'(x', y', z')(i = 0, 1 \cdots n)$ is the intersection of the straight line $PP\prime$ and the fitted plane, substituting $P\prime$ into the plane equation.

$$t = \frac{ax_i + by_i + cz_i - d}{a^2 + b^2 + c^2} \tag{6}$$

Putting t into Equation (5), the equation of the tangent plane of the projected point $P_i'(x', y', z')(i = 0, 1 \cdots n)$ is obtained.

3. Normal vector screening of the projected point. $P_k{}' = \left\{P_1{}', P_2{}' \cdots p_k{}'\right\}$ is the projected point of the point $P_i'(x', y', z')(i = 0, 1 \cdots n)$, so k vectors $P_0'P_1'$, $P_0'P_2'$, $\cdots$, $P_0'P_k'$ are obtained. A comparison should be made between the maximum value of the angle of the vectors and the threshold value. The threshold value can be a default parameter. If the value is greater than the set threshold, then P_0 can be determined to be a boundary point. Similarly, the set of boundary points M can be obtained repeatedly.

Once the boundary information for all operating states of the roller is obtained, the point cloud coordinates of the roller surface contour in the unworn state are compared to the point cloud coordinates of the roller surface contour in the abnormal wear state. If the

Euclidean distance between the contour point cloud of the roller surface in its unworn state and the contour point cloud of the roller in its corresponding abnormal wear state remains almost unchanged, the wear is categorized as normal wear. If the Euclidean distance between the point cloud of the contour of the rubber roller surface in the normal wear condition and the point cloud of the contour of the rubber roller in the corresponding abnormal wear condition is noticeably greater on one side than the other side, it indicates that the condition is due to inadequate rigidity of the support structure. Moreover, if the Euclidean distance between the point cloud contours on both sides is less than the Euclidean distance of the central area, this wear pattern is classified as an anomalous wear condition caused by unequal feeding. By employing this approach, it is possible to ascertain with precision the particular form of deterioration that has occurred in the rubber rollers in question, thus providing a robust basis for the planning of future maintenance and repair operations.

2.2.2. Algorithm for Solving the Mean Value of Rubber Roller Radius

The linear velocity of the rubber rollers' surfaces in a huller can be readily determined by multiplying the rotating speed of the rollers by their radius, assuming ideal operating conditions. However, in practical application, the surfaces of the rollers experience different levels of erosion over time, causing the radius along the axis of rotation to change rather than being constant. This phenomenon enhances the intricacy of precisely determining the true rotational velocity of the huller rollers.

To address this issue, the industry has implemented the notion of 'average roller radius' as an approximate alternative to the continuously fluctuating roller profile radius in practical applications. Hence, it is crucial to precisely ascertain the average radius of a worn roller in order to account for variations in the linear velocity of the actual roller surface. Addressing this issue not only enhances the operational efficiency of the huller, but also carries significant implications for energy management and cost optimization throughout the entire grain processing industry.

This study aims to comprehensively evaluate the surface wear of rubber rollers. To achieve this, an algorithm is developed utilizing a point cloud data-based method to accurately determine the mean radius. This algorithm enables a quantitative analysis of the extent of wear on the rubber rollers. This study employs a laser ranging sensor to accurately capture fault information on the surface of the rubber roller. By utilizing the straight-pass filtering approach, it is possible to systematically capture the accurate information of a specific location on the circle and document its related axial coordinates.

Subsequently, the least squares technique is employed to ascertain the coordinates of the roller center [36]. From these values, the Euclidean distance is computed for every point on the circumference. The comprehensive dispersion of the circumferential data can be visualized through this approach. The precise execution sequence of this technique is outlined in Figure 9. By employing a systematic technological approach, it is possible to ascertain the precise average radius of the worn roller with a high degree of accuracy. These data are dependable and support further wear correction and efficiency optimization.

The experiment utilizes the Intel Core i5-5200 CPU running at 2.50 GHz, 4 GB of RAM, Windows 10 operating system (64-bit), Visual Studio 2019 C++, and the open-source point cloud library PCL 1.8.0.

This section introduces a circle fitting technique based on least squares, which is used to accurately calibrate the centroid coordinates of single-point circumferential point cloud data. This method allows for the calculation of the center and radius of the circle by picking many points at the boundaries of the image, taking into account the cylindrical geometric qualities of the rubber rollers. Least squares is an optimization method focused on identifying the smallest value of the sum of squared distances between the observed data and the predicted data [37]. A circle with center (a_0, b_0) and radius R can be represented as

$$R^2 = (x - a_0)^2 + (y - b_0)^2 \tag{7}$$

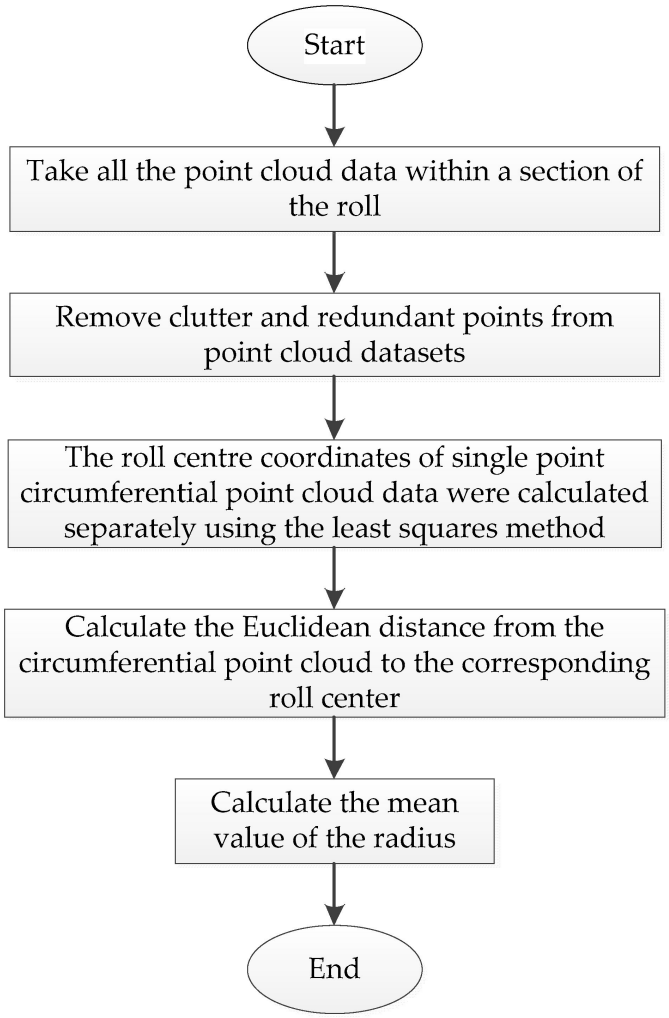

Figure 9. Flowchart of the algorithm for solving the mean value of the radius.

Let $a = -2x_0, b = -2y_0, c = {h_0}^2 + {y_0}^2 - R^2$, then the equation of the circle can also be expressed as

$$x^2 + y^2 + ax + by + c = 0 \tag{8}$$

The set of points at the edge of the rubber roller surface is denoted as (X_i, Y_i) $(i = 1, 2, 3, \ldots N)$, and the sum of squares of errors is denoted as $Q(a, b, c)$ according to the principle of least squares:

$$Q(a, b, c) = \sum_{i=1}^{N} \left({X_i}^2 + {Y_0}^2 + aX_i + bY + c_i\right)^2 \tag{9}$$

$Q(a, b, c)$ is greater than 0, so there is a minimum value greater than or equal to 0, and the maximum value is infinity. The extreme point can be obtained by setting the partial derivatives a, b, and c equal to 0. Afterwards, by comparing the values of the function at all extreme points, the minimum value can be identified. The formulas are as follows:

$$\frac{\partial Q(a, b, c)}{\partial a} = \sum_{i=1}^{N} 2\left(X_i^2 + Y_i^2 + aX_i + bY_i + c\right)X_i = 0 \tag{10}$$

$$\frac{\partial Q(a, b, c)}{\partial b} = \sum_{i=1}^{N} 2\left(X_i^2 + Y_i^2 + aX_i + bY_i + c\right)Y_i = 0 \tag{11}$$

$$\frac{\partial Q(a,b,c)}{\partial c} = \sum_{i=1}^{N} 2\left(X_i^2 + Y_i^2 + aX_i + bY_i + c\right) = 0 \tag{12}$$

Let C, D, E, F, and G be

$$\begin{cases} C = N\sum\limits_{i=1}^{N} X_i^2 - \sum\limits_{i=1}^{N} X_i \sum\limits_{i=1}^{N} X_i \\ D = N\sum\limits_{i=1}^{N} X_i Y_i - \sum\limits_{i=1}^{N} X_i \sum\limits_{i=1}^{N} Y_i \\ E = N\sum\limits_{i=1}^{N} X_i^3 + N\sum\limits_{i=1}^{N} X_i Y_i^2 - \sum\limits_{i=1}^{N} \left(X_i^2 + Y_i^2\right) \sum\limits_{i=1}^{N} X_i \\ F = N\sum\limits_{i=1}^{N} Y_i^2 - \sum\limits_{i=1}^{N} Y_i \sum\limits_{i=1}^{N} Y_i \\ G = N\sum\limits_{i=1}^{N} Y_i^3 + N\sum\limits_{i=1}^{N} X_i^2 Y_i - \sum\limits_{i=1}^{N} \left(X_i^2 + Y_i^2\right) \sum\limits_{i=1}^{N} Y_i \end{cases} \tag{13}$$

Equation (14) can be obtained from Equations (10), (12) and (13):

$$Ca + Db + E = 0 \tag{14}$$

Equation (15) can be obtained from Equations (11)–(13):

$$Da + Fb + G = 0 \tag{15}$$

Then a, b, and c can be found:

$$\begin{cases} a = \frac{DG - EF}{CF - D^2} \\ b = \frac{CG - DE}{D^2 - CF} \\ c = -\frac{\sum_{i=1}^{N}\left(X_i^2 + Y_i^2\right) + a\sum_{i=1}^{N} X_i + b\sum_{i=1}^{N} Y_i}{N} \end{cases} \tag{16}$$

The center (x_0, y_0) and radius R of the circumferential point cloud of a single point on the surface of the rubber roller can then be derived as

$$\begin{cases} \mathrm{x_0} = -\frac{\mathrm{a}}{2} \\ \mathrm{y_0} = -\frac{\mathrm{b}}{2} \\ R = \frac{1}{2}\sqrt{\mathrm{a^2} + \mathrm{b^2} - 4\mathrm{c}} \end{cases} \tag{17}$$

By utilizing the straight-through filtering approach on the point cloud data and leveraging the previously described understanding of least squares circle fitting, it is possible to determine the roller center coordinates of the circumferential point cloud data with remarkable precision. By conducting radius calculations on each specific circumferential point cloud data point, it is possible to ascertain the mean radius of the entire rubber roller. This method establishes a comprehensive database that enables precise adjustment of motor speed, hence ensuring optimal and precise functioning.

2.2.3. Numerical Simulation Method for Roller Spacing

The hulling process in a huller is carried out using the differential gearbox principle, primarily by the interaction between two rubber rollers. One of the rubber rollers remains fixed in place while the other can be modified or moved. Precise control of the dehulling process can be achieved by manipulating the space between the two rollers. These two rollers, driven by mechanical means, revolve in relation to each other. They use the

squeezing and friction between the moving and stationary rollers to remove the outer husk from the paddy. As a result of the ongoing activity, the rubber rollers are consistently in contact with the paddy, leading to variations in the spacing between the two rubber rollers over time.

To study the variation in the roller gap, it is first necessary to select a specified number of points from the datasets obtained from the slow (moving roller) and the fast (stationary roller) rollers. These points serve as typical samples for later analysis and visualization, representing the state of the roller gap at different points in time.

By analyzing the rotational speed relationship between the two rollers, it is evident that the Euclidean distance between each pair of related points, derived from the slow and rapid rollers, can be calculated. The distance being referred to is the direct distance between the two places, which aligns with the physical width of the roller gap. The computation of this distance is achieved using the Euclidean distance formula:

$$r = \sqrt{(x_j - x_i)^2 + (y_j - y_i)^2 + (z_j - z_i)^2} \tag{18}$$

where (x_j, y_j, z_j) and (x_i, y_i, z_i) are the coordinates of the corresponding points on the fixed and movable rollers, respectively.

Considering that the rotational speeds of the two rollers may not be the same, it is necessary to correct the point clouds according to their rotational speed ratios, as shown in Figure 10, to ensure that the calculated Euclidean distances reflect the real roller gap variations.

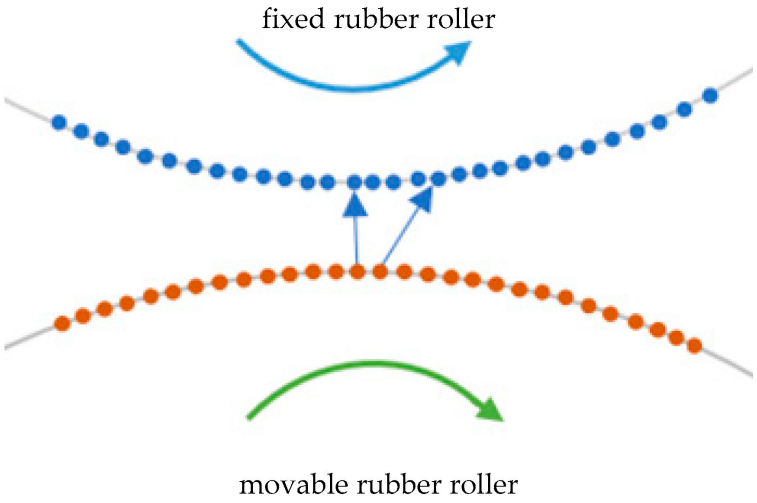

Figure 10. Schematic of the point cloud correspondence between movable and fixed rollers.

To maintain the precision of the study, the point cloud data of the roller gap generated from the initial computation are reused in subsequent studies, signifying the completion of a cycle. The objective of this method is to ascertain the shared pattern of fluctuation in the velocity of the movable and fixed rollers, thereby facilitating a more precise alignment of the motion state of the two rollers. Once the cycles have been established, the study proceeds to gather roller gap data until the required amount of data has been gathered or a satisfactory number of operational cycles have been covered. Ultimately, the gathered roller gap data are visualized using the charts tool to depict the variation in the roller gap over time. This visualization method not only aids in identifying patterns and trends, but also uncovers possible anomalies or cyclical occurrences to facilitate additional data analysis and operational decision making.

Firstly, L' is precisely defined as the Euclidean distance from the center of the movable roller to the corresponding point cloud, which accurately captures the point profile of the movable roller. L'' is defined as the Euclidean distance between the roller center of the fixed roller and the accompanying point cloud. L is defined as the Euclidean distance between

the fixed roller and the movable roller. Therefore, the distance between the fixed roller and the movable roller, known as the roller gap, can be mathematically represented as $I = L - L' - L''$, as illustrated in Figure 11. Since the point cloud data obtained from the surface of the slow and movable roller are evenly distributed, it is possible to determine the data refresh rate by considering the rotational speed and phase information of the rubber rollers. Table 1 displays the precise facts. The subsequent dataset depicts the point cloud of the fixed rollers' surfaces at the following moment, which corresponds to the point cloud of the movable rollers' surfaces at the same moment. By computing the Euclidean distance between these two sets of points, it is feasible to ascertain the roller gap at that specific moment. This measurement serves as a crucial benchmark for evaluating changes in the roller gap.

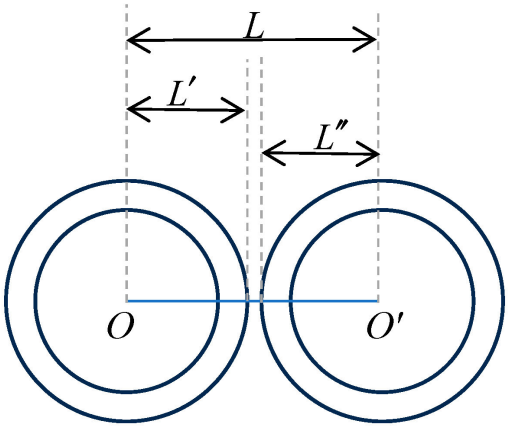

Figure 11. Schematic diagram for visual simulation of roller gap of rubber rollers.

Table 1. Information on the simulated rubber rollers.

Material	Initial Clearance/mm	Roller Rotation Speed/r/min	Simulated Roller Radius/mm	Direction of Rotation Relationship
Fixed rubber roller	1.99	150	15	Relative direction rotation
Movable rubber roller		25	15	

The above steps facilitate the effective processing and analysis of roller gap data, ultimately yielding a visual representation that elucidates the evolution of the roller gap.

The specific steps of the roller gap dynamic simulation algorithm are shown in Figure 12.

The experimental platform utilized for the experiments in this section consists of an Intel Core i5-5200 CPU running at a clock speed of 2.50 GHz, 4 GB of RAM, a 64-bit operating system (Windows 10), Visual Studio 2019 C++ as the programming environment, and the open-source application echarts.

The data visualization tool, echarts, utilizes a JavaScript component library to effectively display data. It is cross-platform, capable of running on many devices such as PCs and mobile devices, and exhibits excellent compatibility [38]. The architecture of echarts primarily comprises the echarts layer and the ZRender layer. The ZRender layer encapsulates the components responsible for rendering visuals, interactive operations, chart animations, and other functionalities.

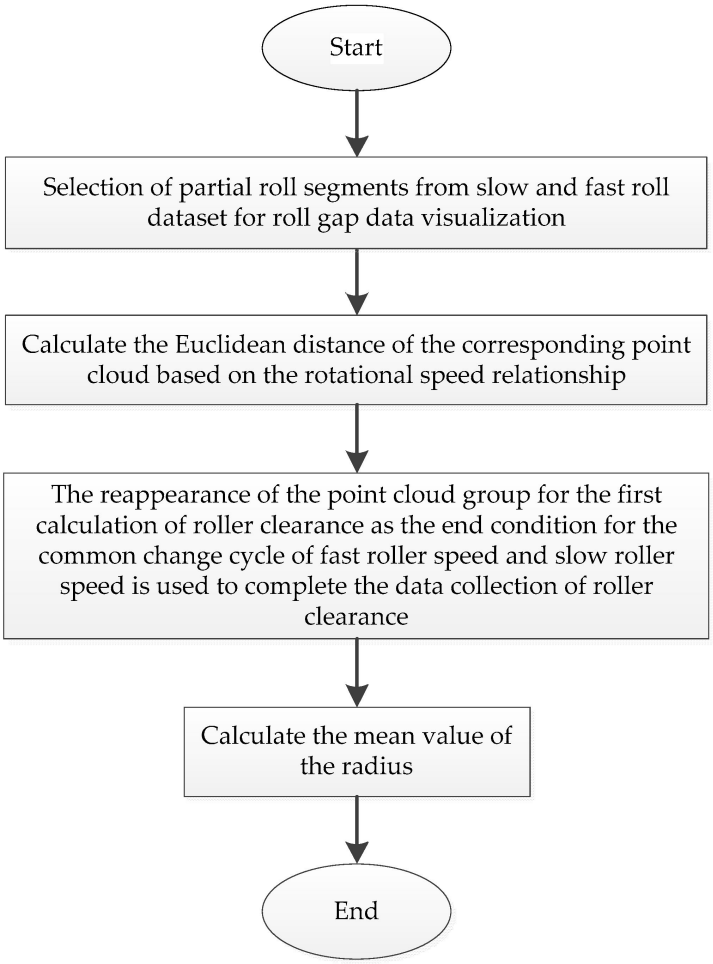

Figure 12. Flowchart of the dynamic simulation algorithm for roller spacing.

3. Results

3.1. Inspection Test Bench Construction

As seen in Figure 13, an experimental platform was constructed to validate the algorithm suggested in this study. The experimental platform is comprised of the computer processing system, the data measurement system, and the control system. The stepper motor lead screw sliding table is where the data measurement system is installed. Table 2 displays the parameters of the workpiece point cloud obtained with the computer processing system and data measurement system. Afterwards, the four operating circumstances that the rice huller encounters in its real operation are simulated using the algorithm from Section 2.

Table 2. ATK-MS53L0M laser distance sensor parameters.

Technical Parameter	Description
Retrieval rate	0.1~100 Hz
Measuring range	40~2000 mm
Measurement precision	±1.6%
Scanning mode	Non-contact
Working temperature	−20 °C~70 °C

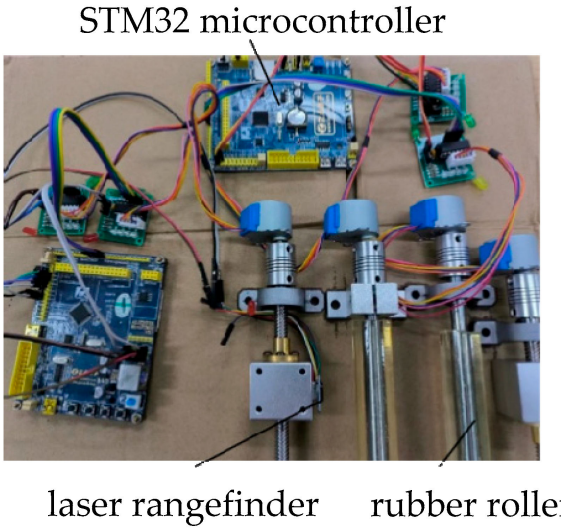

Figure 13. Physical drawing of the inspection test bench.

3.2. Identification of the Working Condition of Rubber Rollers

3.2.1. Abnormal Roller Wear I Working Condition Identification

Figure 14 displays a figure illustrating the unusual erosion of rubber roller I, while Figure 15 presents the point cloud data of the eroded surface of rubber roller I. The faults produced by the abnormal wear I of the rubber roller are identified using the random sampling consistency algorithm. The result displayed in Figure 16 depicts the outcome of applying the RANSAC algorithm to fit a cylindrical surface to the point cloud, representing defects on the surface of rubber roller. By iteratively adjusting the parameters, a distance threshold of 0.05 mm was determined. From the segmentation analysis, it is evident that this method effectively distinguishes between normal surface points and the abnormal wear of type I observed on rubber rollers.

Figure 14. Schematic diagram of abnormal wear I rubber rollers.

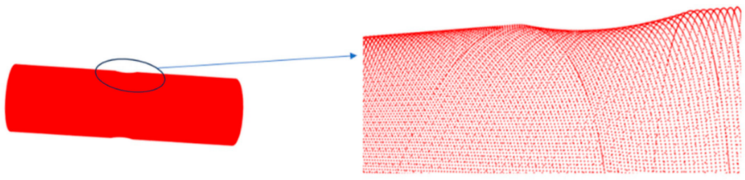

Figure 15. Abnormal wear I roller surface point cloud data.

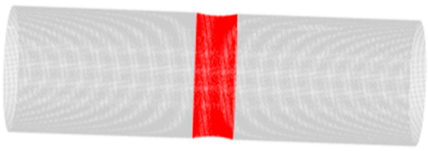

Figure 16. Data after random sampling consistency segmentation.

The RANSAC algorithm effectively distinguishes between normal surface features and anomalies caused by wear in the point cloud data. The illustration illustrates the presence of anomalies in certain regions of the roller, displaying ring and groove patterns that are indicative of localized wear, as expected. The display of the point cloud data enabled the primary cause of wear on the rollers to be identified as localized uneven feeding. The utilization of point cloud data and the RANSAC algorithm allows for the precise evaluation of the condition of the rollers and the establishment of a rational framework for the prevention of potential equipment malfunctions.

3.2.2. Normal Wear Roller Radius Mean Value Solution

As the rubber rollers deteriorate, the speed at which their surfaces move declines, which might negatively impact the ability to remove the husk from the rice. Therefore, it is crucial to promptly and efficiently adjust the motor speed in order to uphold the dehulling efficiency. The rotational speed at a specific place on the roller's surface may be determined by multiplying the rotational speed by the radius of the roller. By adjusting the speed loss accordingly, a uniform linear velocity can be maintained on the roller's surface.

To accomplish this objective, the straight-pass filtering approach is used to gather all single-point circumferential point cloud data of the axial roller segments. These data, along with the examination of the roller surface, provide the essential information needed for speed adjustment. Table 3 displays a portion of the data.

Table 3. Normal wear roller dataset.

X-Axis Position	*Y*-Axis Position	*Z*-Axis Position	Number of Point Clouds
(8.5, 9)	(−13.93, 13.74)	(−14, 14)	128
(9, 10)	(−13.98, 13.71)	(−14, 14)	128
(10, 10.5)	(−14, 13.7)	(−14, 14)	128
(10.5, 11)	(−14, 13.71)	(−14, 14)	128
(11, 12)	(−13.96, 13.74)	(−14, 14)	128
(12, 12.5)	(−13.9, 13.77)	(−14, 14)	128
(12.5, 13.5)	(−13.85, 13.81)	(−14, 14)	128
(13.5, 14.5)	(−13.8, 13.82)	(−14, 14)	128
(14.5, 15)	(−13.74, 13.85)	(−14, 14)	128
(15, 16)	(−13.7, 13.85)	(−14, 14)	128
(16, 16.5)	(−13.67, 13.74)	(−14, 14)	128
(16.5, 17.5)	(−13.64, 13.79)	(−14, 14)	128
(17.5, 18)	(−13.66, 13.74)	(−14, 14)	128
(18, 19)	(−13.66, 13.7)	(−14, 14)	128

Following multiple experiments, the coordinates of the center are determined. Subsequently, the Euclidean distance formula is used to calculate the distance from each point cloud to the roller center of the matching rubber roller.

$$r = \sqrt{(x_j - x_i)^2 + (y_j - y_i)^2 + (z_j - z_i)^2} \tag{19}$$

The average Euclidean distance can be expressed as

$$d = \frac{1}{k} \sum_{j=1}^{k} \parallel P_1^j - P_2^i \parallel \tag{20}$$

The equation can be decomposed further to

$$d = \frac{1}{k} \sum_{j=1}^{k} \sqrt{(x_j - x_i)^2 + (y_j - y_i)^2 + (z_j - z_i)^2} \tag{21}$$

The average Euclidean distance is represented by d. k represents the number of point clouds. P_1^j refers to all single-point circumferential points, while P_2^i represents the point corresponding to the roller center of the single-point circumferential point cloud. (x_i, y_i, z_i) denotes the coordinates of the single-point circumferential point cloud, and (x_i, y_i, z_i) represents the coordinates corresponding to the roller center of the single-point circumferential point cloud. The experimental results are presented in Table 4.

Table 4. Calculation results of mean radius.

Coordinates of the Roller Center	Average Roller Radius	Roller Segment Position	Average Roller Radius of the Roller Section	Measurement Error Value
(8.59, −0.03, 0)	13.87	$8.5 < x_i < 19$	13.86	0.13
(9.38, −0.46, 0)	13.86			0.14
(10.16, −0.08, 0)	13.86			0.14
(10.94, −0.08, 0)	13.87			0.13
(11.72, −0.28, 0)	13.86			0.14
(12.5, −0.13, 0)	13.86			0.14
(13.28, −0.1, 0)	13.86			0.14
(14.06, 0, 0)	13.87			0.13
(14.84, −0.03, 0)	13.87			0.13
(15.63, −0.14, 0)	13.87			0.13
(16.4, −0.28, 0)	13.87			0.13
(17.18, 0.03, 0)	13.86			0.14
(17.96, 0.2, 0)	13.85			0.15
(18.75, 0, −0.33)	13.84			0.16

The calculation of the mean roller radius post-wear enables the necessary speed adjustments to be made in order to maintain a consistent speed for the rubber roller.

3.2.3. Detecting the Working State of Rubber Rollers

Figure 17 displays a physical image of the rubber roller under various working conditions together with the corresponding point cloud data. Figure 17a represents the unworn rubber roller, while Figure 17c gives the corresponding point cloud data. The point cloud data are compared to the wear point cloud data. Figure 17b depicts the rubber roller in its normal wear state, with Figure 17d corresponding to the point cloud data. In the radius direction, there is a certain amount of uniform wear. Figure 17e represents the wear caused by uneven feeding, resulting in non-uniform wear. The corresponding point cloud data are shown in Figure 17g. Figure 17f illustrates an unstable fixed rubber roller device support structure due to excessive vibration caused by wear phenomena. Figure 17e illustrates the wear resulting from uneven feeding, where the rubber roller suffers from non-uniform wear. The corresponding point cloud data can be found in Figure 17g. Figure 17f depicts the wear phenomenon caused by excessive vibration resulting from an unstable support structure of the device used to fix the rubber roller. The corresponding point cloud data can be seen in Figure 17h.

Halfway point cloud data along the roller axis are obtained via straight-pass filtering, which accelerates the acquisition of the contour's running speed. This is achieved by utilizing the point cloud coordinates of the roller surface.

Equation (22) represents the range of straight-pass filtering for the glue roller point cloud data shown in Figure 17a:

$$\begin{cases} 5.26 < x_i < 89.47 \\ -14.99 < y_i < 15 \\ 0 < z_i < 15 \end{cases} \quad (22)$$

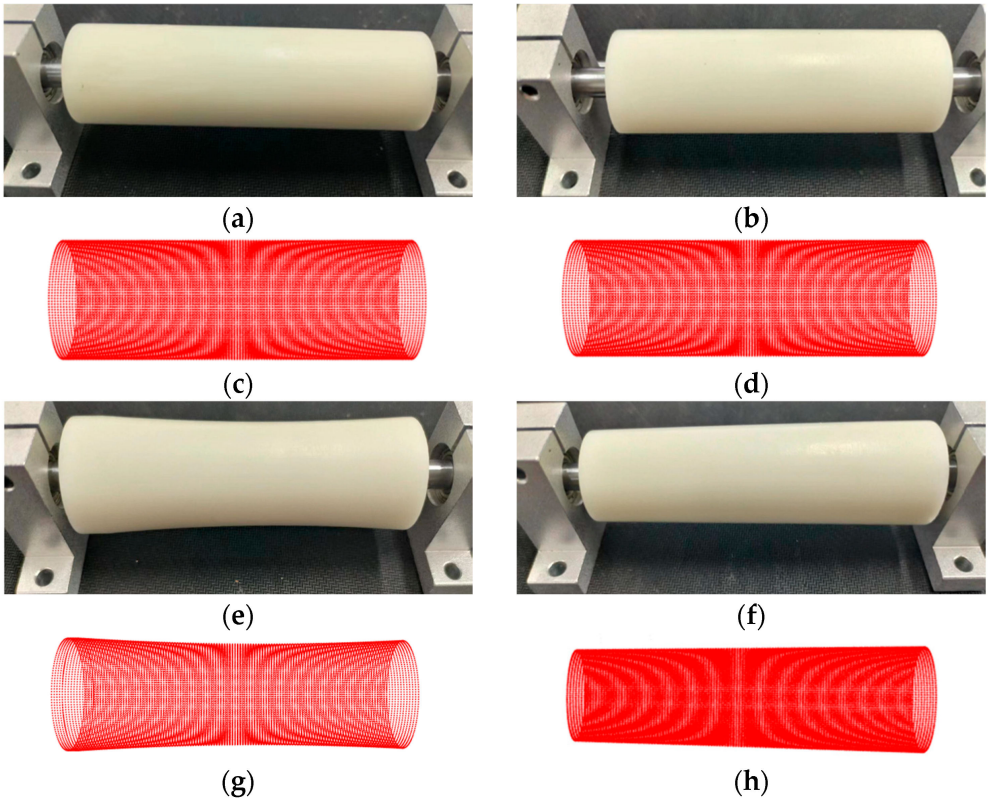

Figure 17. Data of rubber rollers in different working conditions: (**a**) unworn roller; (**b**) normal wear roller; (**c**) unworn roller surface point cloud; (**d**) normal wear roller surface point cloud; (**e**) abnormal wear II rubber roller schematic; (**f**) abnormal wear III roller point cloud data; (**g**) abnormal wear II roller point cloud data; (**h**) abnormal wear III roller surface point cloud data.

Equation (23) represents the range of straight-pass filtering for the glue roller point cloud data shown in Figure 17b:

$$\begin{cases} 5.13 < x_i < 89.74 \\ -13.99 < y_i < 14 \\ 0 < z_i < 14 \end{cases} \tag{23}$$

Equation (24) represents the range of straight-pass filtering for the glue roller point cloud data shown in Figure 17c:

$$\begin{cases} 5.54 < x_i < 89.5 \\ -15 < y_i < 15 \\ 0.03 < z_i < 15 \end{cases} \tag{24}$$

Equation (25) represents the range of straight-pass filtering for the glue roller point cloud data shown in Figure 17d:

$$\begin{cases} 5.26 < x_i < 89.47 \\ -14.47 < y_i < 14.73 \\ 0.14 < z_i < 14.73 \end{cases} \tag{25}$$

Figure 18 depicts the reconstruction of the roller surface contours using point cloud data that have undergone straight-pass filtering. The point cloud data of the unworn roller surface are depicted in Figure 18a. The quantity of points obtained for the unworn roller

surface is decreased from 18,447 to 9288. Figure 18b displays the point cloud data of the roller surface under normal wear conditions. The quantity of points represented by the usual worn roller surface is decreased from 18,221 to 9177. Figure 18e displays the point cloud data of the II roller surface showing anomalous wear. The number of points for the II roller surface subjected to anomalous wear is decreased from 19,464 to 9729. The point cloud data of the unusually worn III roller surface is depicted in Figure 18f. The quantity of point cloud data for the III roller surface subjected to anomalous wear is decreased from 18,447 to 9288. There is a reduction in the number of surface points from 19,464 to 9729, and a decrease from 18,447 to 9288 for the surface point cloud of abnormal wear III rubber roller. Following the implementation of the boundary extraction technique using normal data, Figure 18c displays the point cloud contour for the unworn roller surface. Figure 18d highlights the point cloud contour for the roller surface with normal wear. Figure 18g illustrates the point cloud contour for the roller surface with abnormal wear II. The point cloud contour depicts the surface regions of the III roller that have seen atypical wear. This technique effectively separates the boundary points and provides accurate contour data for further examination of the roller's wear state.

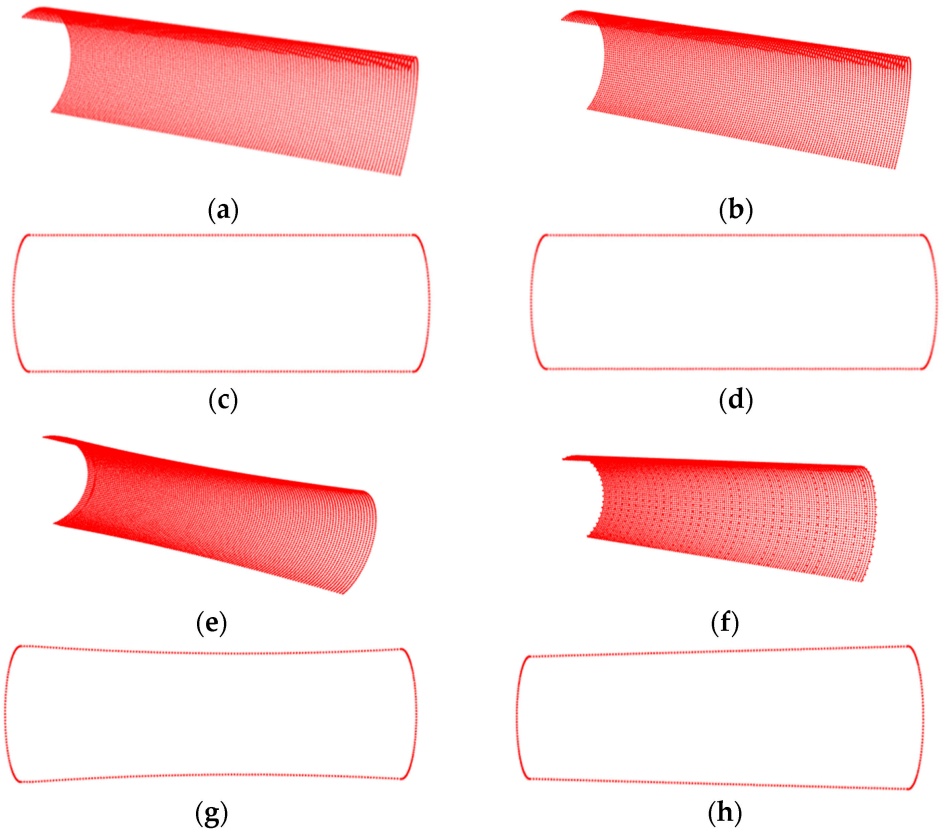

Figure 18. Extraction of point cloud contour of rubber roller surface. (**a**) Point cloud of unworn rubber roller after passthrough filtering; (**b**) point cloud of normally worn rubber roller after passthrough filtering; (**c**) contour of unworn rubber roller surface point cloud; (**d**) contour of normally worn rubber roller surface point cloud; (**e**) abnormal wear II rubber roller schematic after passthrough filtering; (**f**) abnormal wear III rubber roller schematic after passthrough filtering; (**g**) abnormal wear II rubber roller point cloud contour; (**h**) abnormal wear III rubber roller point cloud contour.

The contour adaptive comparison method involves comparing the outer contour of a rubber roller in normal working condition with the inner contour of the same roller in defective working condition. Figure 19 shows the point cloud contour of the surface of the two rubber rollers after the adaptive comparison. By analyzing the change in Euclidean

distance of the point cloud between the two contours, it is possible to determine both the degree of wear and the position of the roller with a high degree of accuracy.

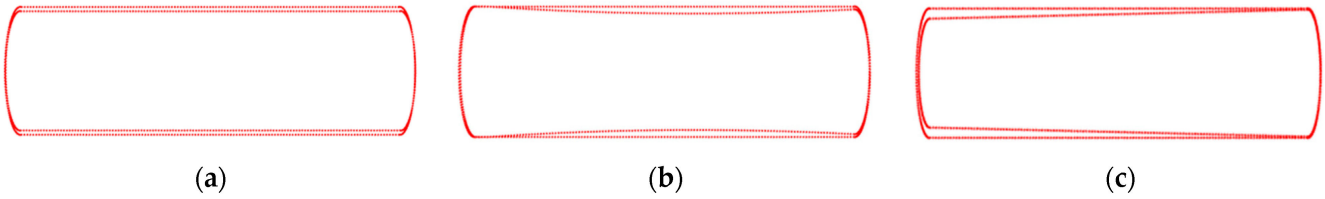

(**a**) (**b**) (**c**)

Figure 19. Adaptive contrast point cloud contours. (**a**) Normal wear adaptive contrast point cloud profile; (**b**) abnormal wear II adaptive contrast point cloud profile; (**c**) abnormal wear III adaptive contrast point cloud profile.

Table 5 presents a portion of the point cloud data obtained from the adaptive comparison profile, specifically the side representing typical wear. This table includes a total of 212 points, while the remaining data can be found in Table A1 in Appendix A. Table 6 shows a portion of the point cloud data obtained from the somewhat abnormal wear II adaptive comparison profile. This table includes a total of 240 points, while the remaining data can be found in Table A2 in Appendix A. Table 7 displays the point cloud data from one side of the partial abnormal wear III adaptive comparison profile. This table includes 212 points, while the remaining data can be found in Table A3 in Appendix A.

Table 5. Normal wear roller profile point cloud information.

Number	Contour of Unworn Roller	Normal Wear Roller Profile	Euclidean Distance
1	(10.54, 15, 0)	(10.54, 14, 0)	1
2	(11.18, 15, 0)	(11.19, 14, 0)	1
3	(11.87, 15, 0)	(11.84, 14, 0)	1
4	(12.5, 15, 0)	(12.51, 14, 0)	1

Table 6. Abnormal wear II roller profile point cloud information.

Number	Contour of Unworn Roller	Abnormal Wear II Profile	Euclidean Distance
1	(10.62, 15, 0)	(10.62, 14.82, 0.31)	0.36
2	(11.28, 15, 0)	(11.28, 14.77, 0.31)	0.38
3	(11.94, 15, 0)	(11.94, 14.73, 0.31)	0.41
4	(12.59, 15, 0)	(12.59, 14.69, 0.31)	0.44

Table 7. Abnormal wear III roller profile point cloud information.

Number	Contour of Unworn Roller	Abnormal Wear III Profile	Euclidean Distance
1	(10.53, 15, 0)	(10.53, 14.78, 0.49)	1.66
2	(11.18, 15, 0)	(11.18, 14.77, 0.49)	1.65
3	(11.84, 15, 0)	(11.84, 14.76, 0.49)	1.63
4	(12.5, 15, 0)	(12.5, 14.74, 0.49)	1.62

Figure 20a depicts two variations in the axial gap contour. The x-axis represents the sequential arrangement of the axial point cloud, while the y-axis represents the Euclidean distance between the two contour point clouds. The Euclidean distance between the contour coordinates of the unworn rubber roller and rubber roller with normal wear remains constant. This confirms that the wear on the rubber roller is within the expected range and can be addressed by making modifications to the speed and roller gap. Figure 20b illustrates a graph depicting the changes in the Euclidean distance between the point cloud profiles of the rubber rollers that are not worn and the rubber rollers that are abnormally worn.

The horizontal coordinates correspond to the sequential arrangement of the point cloud along the axis, while the vertical coordinates indicate the Euclidean distance. Specifically, the Euclidean distances on both sides are shorter than the Euclidean distances of the middle two outlines. The defects in the rubber roller can be categorized as anomalous wear II, resulting from uneven feeding, based on the criteria used to identify wear flaws. By examining the variation in axial clearance of the two profiles shown in Figure 20c, where the horizontal axis represents the order of the axial point cloud and the vertical axis represents the Euclidean distance between the point cloud profiles of the two profiles, it is evident that there is a gradual reduction in the Euclidean distance between the point cloud profiles of the unworn roller and the corresponding point cloud profiles of the abnormal wear III roller. According to the criteria for evaluating wear defects, this change indicates that the unusual wear of the rubber roller (referred to as wear III) is a fault caused by inadequate rigidity in the support structure. It is crucial to quickly strengthen the support framework.

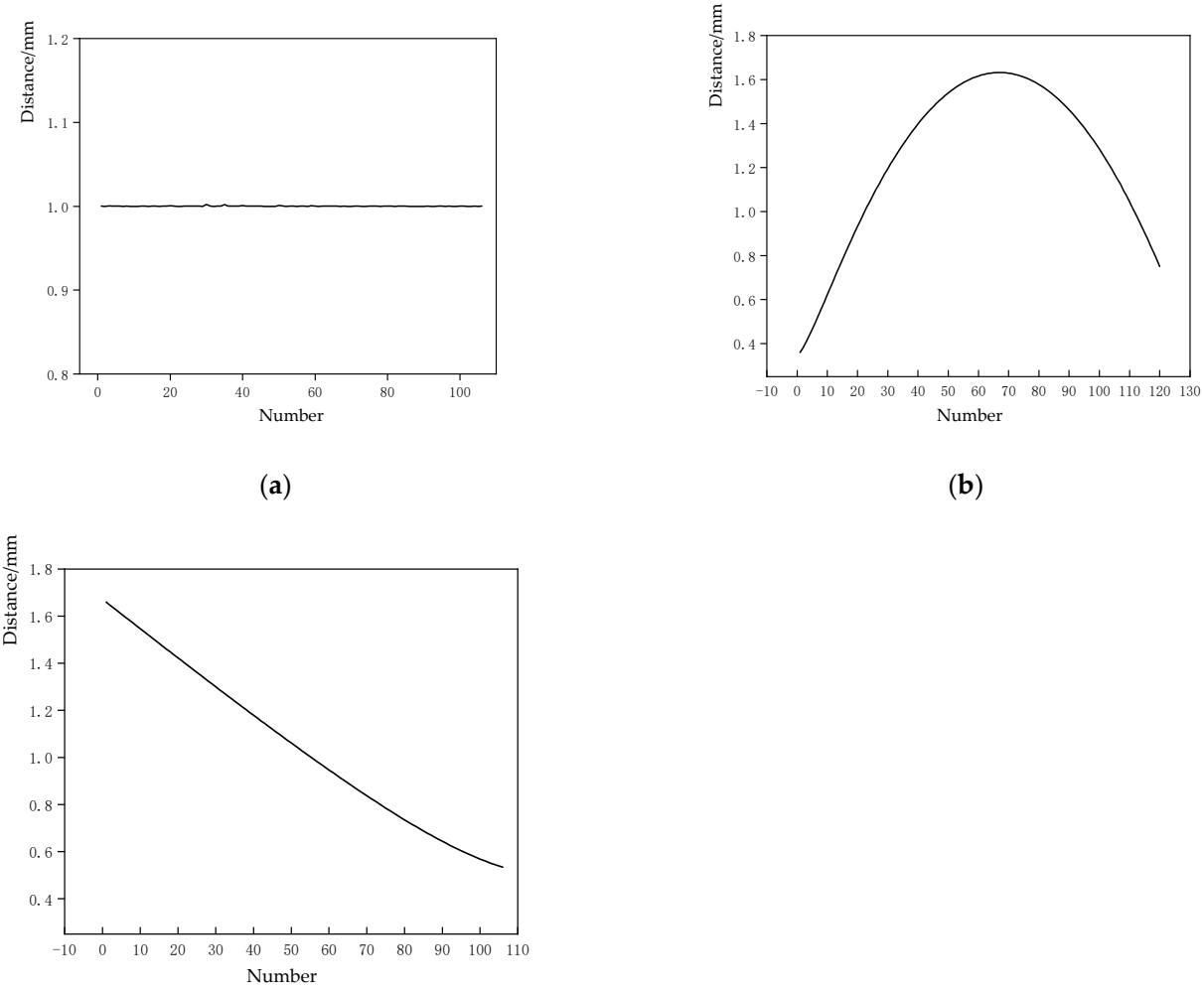

Figure 20. Trends in contour distance. (**a**) Normal wear point cloud contour pitch change; (**b**) abnormal wear II point cloud contour pitch change; (**c**) abnormal wear III point cloud contour pitch change.

3.2.4. Computational Modelling of the Distance between Rollers

Figure 21 displays the point cloud data of the rubber roller in its actual working process, which includes both mobile and fixed rubber rollers. Figure 21a shows the normal wear and tear data for both the mobile and fixed rubber rollers under normal operating conditions. Figure 21b,c depict the uneven feeding state of the rubber roller working

condition, where both the movable and fixed rubber rollers experience excessive wear and tear in the same position. Figure 21d shows that the support structure of a certain roller is not stable, with one side clearly showing more wear than the other side.

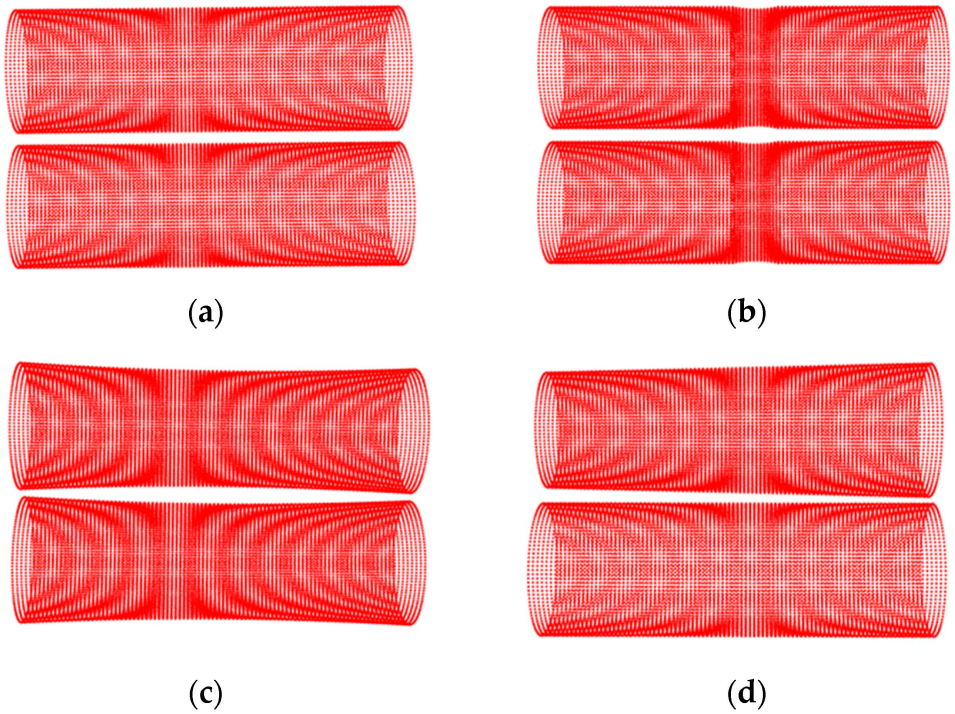

Figure 21. Schematic of roll gap simulation data. (**a**) Schematic of point cloud simulation of normal wear rubber roller spacing; (**b**) abnormal wear I rubber roller pitch simulation point cloud schematic; (**c**) schematic of point cloud simulation of abnormal wear II rubber roller spacing; (**d**) schematic of point cloud simulation of abnormal wear III rubber roller spacing.

The application of straight-through filtering is employed to extract a specific portion of the roller surface data point cloud simulation. This part corresponds to the dynamic variations in the spacing of the roller, as depicted in Figure 22. The extracted data represent the point cloud data for the roller section affected by normal wear.

Equation (26) represents the operational range of the straight-through filter for the dataset shown in Figure 21a:

$$\begin{cases} 40.38 < x_i < 50 \\ -34.9 < y_i < 14 \\ -36.87 < z_i < 14 \end{cases} \tag{26}$$

Equation (27) represents the operational range of the straight-through filter for the dataset shown in Figure 21b:

$$\begin{cases} 42.39 < x_i < 57.6 \\ -30.91 < y_i < 15 \\ -39.37 < z_i < 15 \end{cases} \tag{27}$$

Equation (28) represents the operational range of the straight-through filter for the dataset shown in Figure 21c:

$$\begin{cases} 40.19 < x_i < 65.17 \\ -37.91 < y_i < 13.54 \\ -39.37 < z_i < 13.94 \end{cases} \tag{28}$$

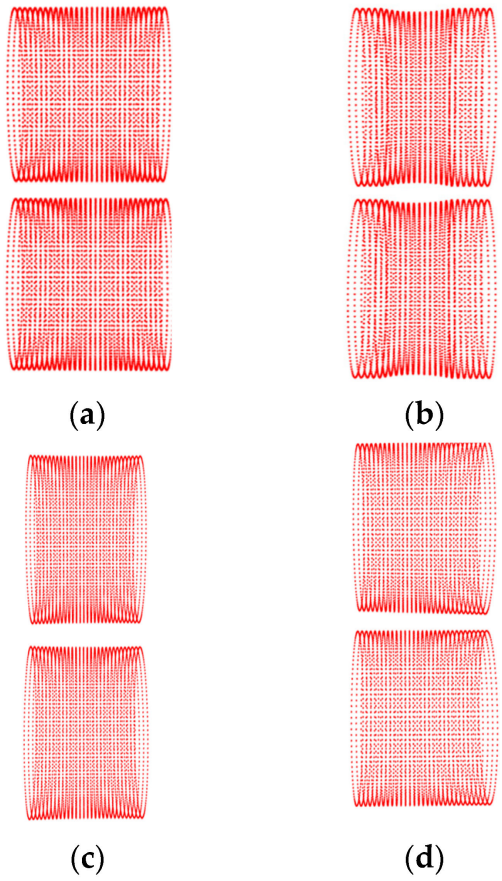

Figure 22. Point cloud data of roller segments in different operating conditions. (**a**) Normal wear roller segment point cloud data; (**b**) abnormal wear I roller segment point cloud data; (**c**) abnormal wear II roller segment point cloud data; (**d**) abnormal wear III roller segment point cloud data.

Equation (29) represents the operational range of the straight-through filter for the dataset shown in Figure 21d:

$$\begin{cases} 40.14 < x_i < 50 \\ -34.91 < y_i < 13.5 \\ -34.87 < z_i < 13.5 \end{cases} \quad (29)$$

The segment underwent straight-pass filtering to obtain circumferential point clouds consisting of individual points. The single-point point cloud data were used to simulate the variations in the roller gap of the rubber rollers. The resultant data are available in Tables A4–A7 in Appendix A.

The discrepancy between the stationary roller and the mobile roller is depicted through data visualizations using echarts, utilizing the interconnectedness of their respective rotational velocities. This picture functions as a point of comparison for identifying any alterations in the space between the rollers.

Figure 23 shows point cloud data being used effectively to accomplish precise simulation of roller gap dynamics. Figure 23a illustrates the changes in the distance between the rollers in the axial (40.38, 50) section of a roller that is typically worn. To keep a consistent space between rollers, it is important to modify the location of the movable roller based on the level of wear. Figure 23b,c display graphs illustrating the changes in gap size for rollers with abnormal wear I and II in the axial direction. The rollers are excessively worn in specific areas, and it is necessary to adjust the feeding system to ensure uniform feeding. Figure 23d displays the diagram of a dynamic simulation depicting aberrant wear on rubber roller III in the axial direction. This occurs specifically in the roller section with

coordinates (40.14, 50). The wear on the left side is considerably more pronounced than that on the right side, thereby requiring prompt repair of the huller.

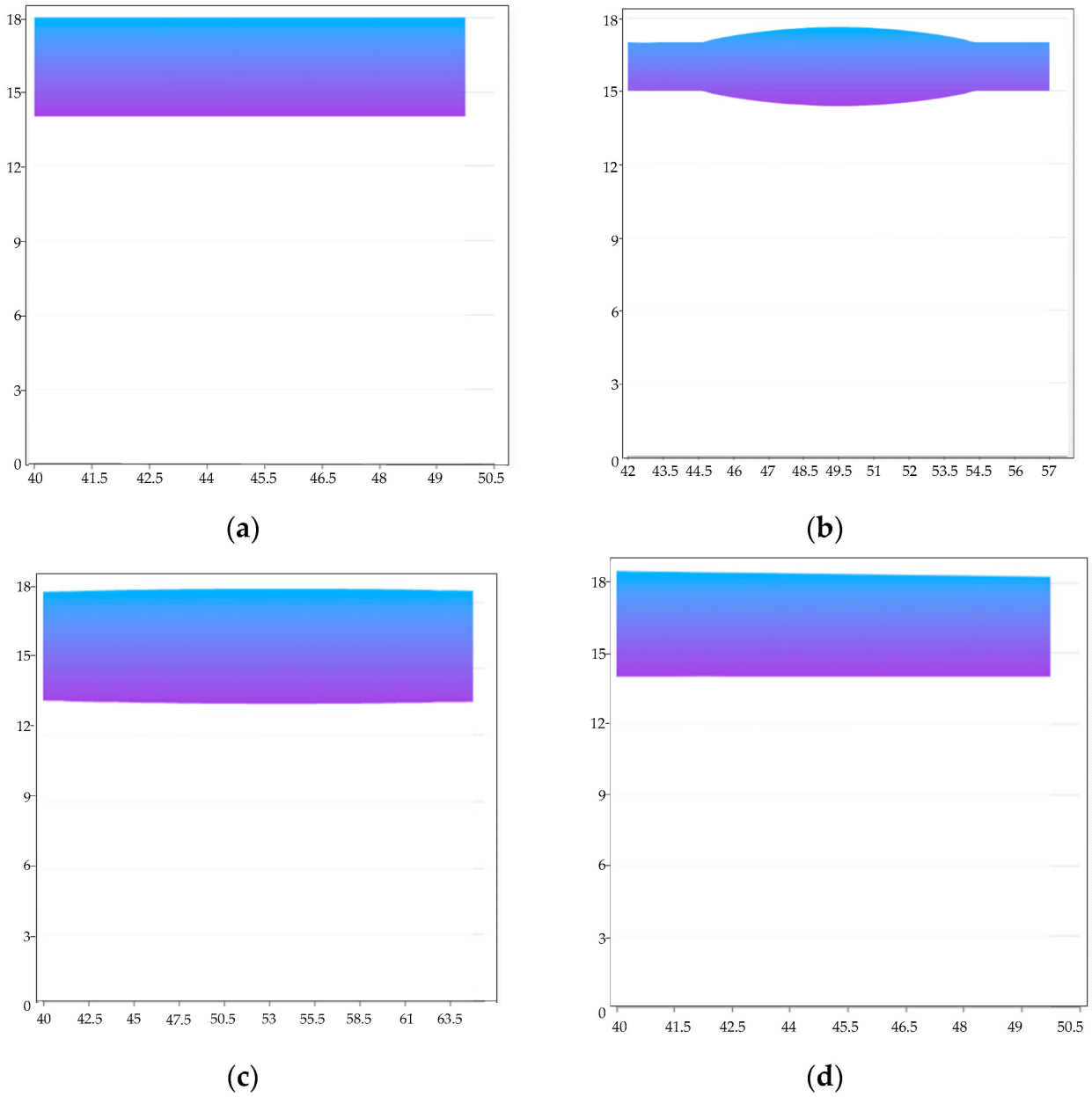

Figure 23. Dynamic simulation of roller spacing. (**a**) Visualization of numerical simulation of normal wear roller spacing; (**b**) visualization of numerical simulation of abnormal wear I roller spacing; (**c**) visualization of numerical simulation of abnormal wear II roller spacing; (**d**) visualization of numerical simulation of abnormal wear III roller spacing.

4. Conclusions

This study proposes the use of laser ranging to collect point cloud data for real-time online monitoring of grinding roller wear in the grain processing industry. Once the point cloud data are processed, the working status of the huller is determined as follows:

1. The rubber roller surface point cloud data defect identification problem is addressed by proposing the use of a random sampling consistency segmentation algorithm and normal-based adaptive boundary extraction algorithm. This method enables the identification and comparison of the type of defects on the rubber roller surface,

hence effectively solving the problem of identifying the condition of defects in the production process.

2. To address the rubber roller speed compensation issue, a technique is provided for calculating the radius wear of the normal wear rubber roller using the rubber roller radius mean value solving algorithm of the huller. This method successfully resolves the speed compensation problem of the huller in the manufacturing process.
3. The suggested roller spacing numerical simulation technique enables real-time monitoring of dynamic changes in roller spacing, therefore successfully reducing undesired losses and breakdowns in the manufacturing process.

The approach presented in this work is validated using a self-constructed experimental platform to conduct tests and confirm its efficacy. To enhance the performance of the future huller in actual production practice, the development will be conducted extensively using several batches of material and will include the analysis of wear properties in combination with micro-morphological examination. This will enable the automatic adjustment of research parameters, so further advancing the intelligent level of the grain processing industry.

Author Contributions: Conceptualization, Z.W. and Z.Z.; methodology, X.L.; software, T.J.; validation, T.J.; formal analysis, B.Z.; investigation, Y.Z.; resources, T.J.; data curation, T.J.; writing—original draft preparation, T.J.; writing—review and editing, T.J.; visualization, X.H.; supervision, Z.Z.; project administration, Z.W.; funding acquisition, Z.W. All authors have read and agreed to the published version of the manuscript.

Funding: This research was funded by the Science and Technology Project of Henan Province in China [Grant No. 222103810085 and No. 232103810085].

Institutional Review Board Statement: Not applicable.

Informed Consent Statement: Not applicable.

Data Availability Statement: All data are provided in both the main manuscript and Appendix A.

Conflicts of Interest: The authors declare no conflicts of interest.

Appendix A

Table A1. Normal wear roller profile point cloud information.

Normal Wear Rubber Roller Points Cloud Contour Coordinates	Point Cloud Contour Coordinates of Unworn Roller	Euclidean Distance for the Corresponding Coordinates
(10.54, 14, 0)	(10.53, 15, 0)	1
(11.18, 14, 0)	(11.18, 15, 0)	1
(11.87, 14, 0)	(11.84, 15, 0)	1
(12.51, 14, 0)	(12.5, 15, 0)	1
(13.15, 14, 0)	(13.16, 15, 0)	1
(13.81, 14, 0)	(13.82, 15, 0)	1
(14.47, 14, 0)	(14.47, 15, 0)	1
(15.14, 14, 0)	(15.13, 15, 0)	1
(15.79, 14, 0)	(15.79, 15, 0)	1
(16.45, 14, 0)	(16.45, 15, 0)	1
(17.11, 14, 0)	(17.11, 15, 0)	1
(17.77, 14, 0)	(17.76, 15, 0)	1
(18.43, 14, 0)	(18.42, 15, 0)	1
(19.08, 14, 0)	(19.08, 15, 0)	1
(19.73, 14, 0)	(19.74, 15, 0)	1
(20.38, 14, 0)	(20.39, 15, 0)	1
(21.05, 14, 0)	(21.05, 15, 0)	1

Table A1. *Cont.*

Normal Wear Rubber Roller Points Cloud Contour Coordinates	Point Cloud Contour Coordinates of Unworn Roller	Euclidean Distance for the Corresponding Coordinates
(21.71, 14, 0)	(21.71, 15, 0)	1
(22.36, 14, 0)	(22.37, 15, 0)	1
(23.06, 14, 0)	(23.03, 15, 0)	1
(23.68, 14, 0)	(23.68, 15, 0)	1
(24.34, 14, 0)	(24.34, 15, 0)	1
(25, 14, 0)	(25, 15, 0)	1
(25.64, 14, 0)	(25.66, 15, 0)	1
(26.31, 14, 0)	(26.32, 15, 0)	1
(26.98, 14, 0)	(26.97, 15, 0)	1
(27.64, 14, 0)	(27.63, 15, 0)	1
(28.29, 14, 0)	(28.29, 15, 0)	1
(28.95, 14, 0)	(28.95, 15, 0)	1
(29.67, 14, 0)	(29.61, 15, 0)	1
(30.28, 14, 0)	(30.26, 15, 0)	1
(30.92, 14, 0)	(30.92, 15, 0)	1
(31.57, 14, 0)	(31.58, 15, 0)	1
(32.23, 14, 0)	(32.24, 15, 0)	1
(32.83, 14, 0)	(32.89, 15, 0)	1
(33.55, 14, 0)	(33.55, 15, 0)	1
(34.22, 14, 0)	(34.21, 15, 0)	1
(34.86, 14, 0)	(34.87, 15, 0)	1
(35.53, 14, 0)	(35.53, 15, 0)	1
(36.15, 14, 0)	(36.18, 15, 0)	1
(36.85, 14, 0)	(36.84, 15, 0)	1
(37.52, 14, 0)	(37.5, 15, 0)	1
(38.15, 14, 0)	(38.16, 15, 0)	1
(38.81, 14, 0)	(38.82, 15, 0)	1
(39.48, 14, 0)	(39.47, 15, 0)	1
(40.13, 14, 0)	(40.13, 15, 0)	1
(40.79, 14, 0)	(40.79, 15, 0)	1
(41.45, 14, 0)	(41.45, 15, 0)	1
(42.11, 14, 0)	(42.11, 15, 0)	1
(42.72, 14, 0)	(42.76, 15, 0)	1
(43.45, 14, 0)	(43.42, 15, 0)	1
(44.08, 14, 0)	(44.08, 15, 0)	1
(44.73, 14, 0)	(44.74, 15, 0)	1
(45.38, 14, 0)	(45.39, 15, 0)	1
(46.05, 14, 0)	(46.05, 15, 0)	1
(46.71, 14, 0)	(46.71, 15, 0)	1
(47.36, 14, 0)	(47.37, 15, 0)	1
(48.03, 14, 0)	(48.03, 15, 0)	1
(48.72, 14, 0)	(48.68, 15, 0)	1
(49.36, 14, 0)	(49.34, 15, 0)	1
(50, 14, 0)	(50, 15, 0)	1
(50.64, 14, 0)	(50.66, 15, 0)	1
(51.31, 14, 0)	(51.32, 15, 0)	1
(51.98, 14, 0)	(51.97, 15, 0)	1
(52.64, 14, 0)	(52.63, 15, 0)	1
(53.29, 14, 0)	(53.29, 15, 0)	1
(53.95, 14, 0)	(53.95, 15, 0)	1
(54.6, 14, 0)	(54.61, 15, 0)	1
(55.26, 14, 0)	(55.26, 15, 0)	1
(55.92, 14, 0)	(55.92, 15, 0)	1
(56.57, 14, 0)	(56.58, 15, 0)	1

Table A1. *Cont.*

Normal Wear Rubber Roller Points Cloud Contour Coordinates	Point Cloud Contour Coordinates of Unworn Roller	Euclidean Distance for the Corresponding Coordinates
(57.23, 14, 0)	(57.24, 15, 0)	1
(57.89, 14, 0)	(57.89, 15, 0)	1
(58.55, 14, 0)	(58.55, 15, 0)	1
(59.22, 14, 0)	(59.21, 15, 0)	1
(59.86, 14, 0)	(59.87, 15, 0)	1
(60.52, 14, 0)	(60.53, 15, 0)	1
(61.18, 14, 0)	(61.18, 15, 0)	1
(61.85, 14, 0)	(61.84, 15, 0)	1
(62.49, 14, 0)	(62.5, 15, 0)	1
(63.15, 14, 0)	(63.16, 15, 0)	1
(63.82, 14, 0)	(63.82, 15, 0)	1
(64.46, 14, 0)	(64.47, 15, 0)	1
(65.14, 14, 0)	(65.13, 15, 0)	1
(65.78, 14, 0)	(65.79, 15, 0)	1
(66.45, 14, 0)	(66.45, 15, 0)	1
(67.11, 14, 0)	(67.11, 15, 0)	1
(67.77, 14, 0)	(67.76, 15, 0)	1
(68.42, 14, 0)	(68.42, 15, 0)	1
(69.08, 14, 0)	(69.08, 15, 0)	1
(69.73, 14, 0)	(69.74, 15, 0)	1
(70.39, 14, 0)	(70.39, 15, 0)	1
(71.05, 14, 0)	(71.05, 15, 0)	1
(71.71, 14, 0)	(71.71, 15, 0)	1
(72.36, 14, 0)	(72.37, 15, 0)	1
(73.03, 14, 0)	(73.03, 15, 0)	1
(73.69, 14, 0)	(73.68, 15, 0)	1
(74.34, 14, 0)	(74.34, 15, 0)	1
(75, 14, 0)	(75, 15, 0)	1
(75.65, 14, 0)	(75.66, 15, 0)	1
(76.31, 14, 0)	(76.32, 15, 0)	1
(76.97, 14, 0)	(76.97, 15, 0)	1
(77.63, 14, 0)	(77.63, 15, 0)	1
(78.29, 14, 0)	(78.29, 15, 0)	1
(78.95, 14, 0)	(78.95, 15, 0)	1
(79.6, 14, 0)	(79.61, 15, 0)	1

Table A2. Abnormal wear II rubber roller profile point cloud information.

Abnormal Wear II Rubber Roller Point Cloud Profile Coordinates	Point Cloud Contour Coordinates of Unworn Roller	Euclidean Distance for the Corresponding Coordinates
(10.62, 14.82, 0.31)	(10.62, 15, 0)	0.36
(11.28, 14.78, 0.31)	(11.28, 15, 0)	0.38
(11.94, 14.73, 0.31)	(11.92, 15, 0)	0.41
(12.59, 14.69, 0.31)	(12.59, 15, 0)	0.44
(13.25, 14.65, 0.31)	(13.26, 15, 0)	0.46
(13.91, 14.61, 0.31)	(13.91, 15, 0)	0.5
(14.56, 14.57, 0.31)	(14.57, 15, 0)	0.53
(15.22, 14.53, 0.3)	(15.22, 15, 0)	0.56
(15.88, 14.49, 0.3)	(15.88, 15, 0)	0.59
(16.53, 14.46, 0.3)	(16.54, 15, 0)	0.62
(17.19, 14.42, 0.3)	(17.19, 15, 0)	0.65
(17.85, 14.38, 0.3)	(17.83, 15, 0)	0.69

Table A2. *Cont.*

Abnormal Wear II Rubber Roller Point Cloud Profile Coordinates	Point Cloud Contour Coordinates of Unworn Roller	Euclidean Distance for the Corresponding Coordinates
(18.5, 14.35, 0.3)	(18.5, 15, 0)	0.72
(19.16, 14.31, 0.3)	(19.16, 15, 0)	0.75
(19.82, 14.28, 0.3)	(19.81, 15, 0)	0.78
(20.47, 14.24, 0.3)	(20.47, 15, 0)	0.81
(21.13, 14.21, 0.3)	(21.13, 15, 0)	0.84
(21.79, 14.18, 0.3)	(21.79, 15, 0)	0.87
(22.44, 14.15, 0.3)	(22.44, 15, 0)	0.9
(23.1, 14.12, 0.3)	(23.1, 15, 0)	0.93
(23.76, 14.09, 0.3)	(23.75, 15, 0)	0.96
(24.41, 14.06, 0.29)	(24.42, 15, 0)	0.99
(25.07, 14.03, 0.29)	(25, 15, 0)	1.02
(25.73, 14, 0.29)	(25.73, 15, 0)	1.04
(26.39, 13.97, 0.29)	(26.39, 15, 0)	1.07
(27.04, 13.94, 0.29)	(26.98, 15, 0)	1.1
(27.7, 13.92, 0.29)	(27.68, 15, 0)	1.12
(28.36, 13.89, 0.29)	(28.35, 15, 0)	1.15
(29.01, 13.87, 0.29)	(28.97, 15, 0)	1.17
(29.67, 13.84, 0.29)	(29.68, 15, 0)	1.19
(30.33, 13.82, 0.29)	(30.32, 15, 0)	1.22
(30.99, 13.79, 0.29)	(30.98, 15, 0)	1.24
(31.64, 13.77, 0.29)	(31.65, 15, 0)	1.26
(32.3, 13.75, 0.29)	(32.3, 15, 0)	1.28
(32.96, 13.73, 0.29)	(32.95, 15, 0)	1.3
(33.62, 13.71, 0.29)	(33.62, 15, 0)	1.32
(34.27, 13.69, 0.29)	(34.26, 15, 0)	1.34
(34.93, 13.67, 0.29)	(34.92, 15, 0)	1.36
(35.59, 13.65, 0.29)	(35.58, 15, 0)	1.38
(36.24, 13.63, 0.29)	(36.24, 15, 0)	1.4
(36.9, 13.61, 0.29)	(36.84, 15, 0)	1.42
(37.56, 13.6, 0.28)	(37.5, 15, 0)	1.43
(38.22, 13.58, 0.28)	(38.22, 15, 0)	1.45
(38.87, 13.57, 0.28)	(38.88, 15, 0)	1.46
(39.53, 13.55, 0.28)	(39.54, 15, 0)	1.48
(40.19, 13.54, 0.28)	(40.18, 15, 0)	1.49
(40.85, 13.52, 0.28)	(40.85, 15, 0)	1.5
(41.5, 13.51, 0.28)	(41.5, 15, 0)	1.52
(42.16, 13.5, 0.28)	(42.16, 15, 0)	1.53
(42.82, 13.49, 0.28)	(42.82, 15, 0)	1.54
(43.48, 13.48, 0.28)	(43.48, 15, 0)	1.55
(44.14, 13.47, 0.28)	(44.13, 15, 0)	1.56
(44.79, 13.46, 0.28)	(44.78, 15, 0)	1.57
(45.45, 13.45, 0.28)	(45.47, 15, 0)	1.58
(46.11, 13.44, 0.28)	(46.11, 15, 0)	1.59
(46.77, 13.43, 0.28)	(46.76, 15, 0)	1.59
(47.42, 13.43, 0.28)	(47.42, 15, 0)	1.6
(48.08, 13.42, 0.28)	(48.03, 15, 0)	1.61
(48.74, 13.41, 0.28)	(48.74, 15, 0)	1.61
(49.4, 13.41, 0.28)	(49.39, 15, 0)	1.62
(50.05, 13.4, 0.28)	(50, 15, 0)	1.62
(50.71, 13.4, 0.28)	(50.72, 15, 0)	1.62
(51.37, 13.4, 0.28)	(51.38, 15, 0)	1.63
(52.03, 13.4, 0.28)	(51.99, 15, 0)	1.63
(52.68, 13.39, 0.28)	(52.68, 15, 0)	1.63
(53.34, 13.39, 0.28)	(53.35, 15, 0)	1.63

Table A2. *Cont.*

Abnormal Wear II Rubber Roller Point Cloud Profile Coordinates	Point Cloud Contour Coordinates of Unworn Roller	Euclidean Distance for the Corresponding Coordinates
(54, 13.39, 0.28)	(54, 15, 0)	1.63
(54.66, 13.39, 0.28)	(54.65, 15, 0)	1.63
(55.32, 13.39, 0.28)	(55.32, 15, 0)	1.63
(55.97, 13.4, 0.28)	(55.97, 15, 0)	1.63
(56.63, 13.4, 0.28)	(56.65, 15, 0)	1.63
(57.29, 13.4, 0.28)	(57.28, 15, 0)	1.62
(57.95, 13.4, 0.28)	(57.95, 15, 0)	1.62
(58.6, 13.41, 0.28)	(58.6, 15, 0)	1.62
(59.26, 13.41, 0.28)	(59.26, 15, 0)	1.61
(59.92, 13.42, 0.28)	(59.91, 15, 0)	1.61
(60.58, 13.43, 0.28)	(60.56, 15, 0)	1.6
(61.23, 13.43, 0.28)	(61.24, 15, 0)	1.59
(61.89, 13.44, 0.28)	(61.9, 15, 0)	1.59
(62.55, 13.45, 0.28)	(62.54, 15, 0)	1.58
(63.21, 13.46, 0.28)	(63.21, 15, 0)	1.57
(63.86, 13.47, 0.28)	(63.86, 15, 0)	1.56
(64.52, 13.48, 0.28)	(64.52, 15, 0)	1.55
(65.18, 13.49, 0.28)	(65.18, 15, 0)	1.54
(65.84, 13.5, 0.28)	(65.85, 15, 0)	1.53
(66.5, 13.51, 0.28)	(66.5, 15, 0)	1.52
(67.15, 13.52, 0.28)	(67.15, 15, 0)	1.5
(67.81, 13.54, 0.28)	(67.82, 15, 0)	1.49
(68.47, 13.55, 0.28)	(68.45, 15, 0)	1.48
(69.13, 13.57, 0.28)	(69.12, 15, 0)	1.46
(69.78, 13.58, 0.28)	(69.78, 15, 0)	1.45
(70.44, 13.6, 0.28)	(70.45, 15, 0)	1.43
(71.1, 13.61, 0.29)	(71.1, 15, 0)	1.42
(71.76, 13.63, 0.29)	(71.75, 15, 0)	1.4
(72.41, 13.65, 0.29)	(72.42, 15, 0)	1.38
(73.07, 13.67, 0.29)	(73.06, 15, 0)	1.36
(73.73, 13.69, 0.29)	(73.72, 15, 0)	1.34
(74.38, 13.71, 0.29)	(74.38, 15, 0)	1.32
(75.04, 13.73, 0.29)	(75, 15, 0)	1.3
(75.7, 13.75, 0.29)	(75.67, 15, 0)	1.28
(76.36, 13.77, 0.29)	(76.36, 15, 0)	1.26
(77.01, 13.79, 0.29)	(77.01, 15, 0)	1.24
(77.67, 13.82, 0.29)	(77.68, 15, 0)	1.22
(78.33, 13.84, 0.29)	(78.32, 15, 0)	1.19
(78.99, 13.87, 0.29)	(78.97, 15, 0)	1.17
(79.64, 13.89, 0.29)	(79.65, 15, 0)	1.15
(80.3, 13.92, 0.29)	(80.23, 15, 0)	1.12
(80.96, 13.94, 0.29)	(80.95, 15, 0)	1.1
(81.61, 13.97, 0.29)	(81.61, 15, 0)	1.07
(82.27, 14, 0.29)	(82.27, 15, 0)	1.04
(82.93, 14.03, 0.29)	(82.94, 15, 0)	1.02
(83.59, 14.06, 0.29)	(83.56, 15, 0)	0.99
(84.24, 14.09, 0.3)	(84.25, 15, 0)	0.96
(84.9, 14.12, 0.3)	(84.88, 15, 0)	0.93
(85.56, 14.15, 0.3)	(85.54, 15, 0)	0.9
(86.21, 14.18, 0.3)	(86.21, 15, 0)	0.87
(86.87, 14.21, 0.3)	(86.87, 15, 0)	0.84
(87.53, 14.24, 0.3)	(87.52, 15, 0)	0.81
(88.18, 14.28, 0.3)	(88.18, 15, 0)	0.78
(88.84, 14.31, 0.3)	(88.84, 15, 0)	0.75

Table A3. Abnormal wear III rubber roller profile point cloud information.

Abnormal Wear III Rubber Roller Point Cloud Profile Coordinates	Point Cloud Contour Coordinates of Unworn Roller	Euclidean Distance for the Corresponding Coordinates
(10.53, 14.78, 0.49)	(10.53, 15, 0)	1.66
(11.18, 14.77, 0.49)	(11.18, 15, 0)	1.65
(11.84, 14.76, 0.49)	(11.84, 15, 0)	1.63
(12.5, 14.74, 0.49)	(12.5, 15, 0)	1.62
(13.16, 14.73, 0.49)	(13.16, 15, 0)	1.61
(13.82, 14.72, 0.49)	(13.82, 15, 0)	1.6
(14.47, 14.7, 0.48)	(14.47, 15, 0)	1.58
(15.13, 14.69, 0.48)	(15.13, 15, 0)	1.57
(15.79, 14.68, 0.48)	(15.79, 15, 0)	1.56
(16.45, 14.66, 0.48)	(16.45, 15, 0)	1.55
(17.11, 14.65, 0.48)	(17.11, 15, 0)	1.53
(17.76, 14.64, 0.48)	(17.76, 15, 0)	1.52
(18.42, 14.62, 0.48)	(18.42, 15, 0)	1.51
(19.08, 14.61, 0.48)	(19.08, 15, 0)	1.5
(19.74, 14.6, 0.48)	(19.74, 15, 0)	1.48
(20.39, 14.58, 0.48)	(20.39, 15, 0)	1.47
(21.05, 14.57, 0.48)	(21.05, 15, 0)	1.46
(21.71, 14.56, 0.48)	(21.71, 15, 0)	1.45
(22.37, 14.54, 0.48)	(22.37, 15, 0)	1.43
(23.03, 14.53, 0.48)	(23.03, 15, 0)	1.42
(23.68, 14.52, 0.48)	(23.68, 15, 0)	1.41
(24.34, 14.51, 0.48)	(24.34, 15, 0)	1.4
(25, 14.49, 0.48)	(25, 15, 0)	1.39
(25.66, 14.48, 0.48)	(25.66, 15, 0)	1.37
(26.32, 14.47, 0.48)	(26.32, 15, 0)	1.36
(26.97, 14.45, 0.48)	(26.97, 15, 0)	1.35
(27.63, 14.44, 0.48)	(27.63, 15, 0)	1.34
(28.29, 14.43, 0.48)	(28.29, 15, 0)	1.32
(28.95, 14.41, 0.48)	(28.95, 15, 0)	1.31
(29.61, 14.4, 0.47)	(29.61, 15, 0)	1.3
(30.26, 14.39, 0.47)	(30.26, 15, 0)	1.29
(30.92, 14.37, 0.47)	(30.92, 15, 0)	1.28
(31.58, 14.36, 0.47)	(31.58, 15, 0)	1.26
(32.24, 14.35, 0.47)	(32.24, 15, 0)	1.25
(32.89, 14.33, 0.47)	(32.89, 15, 0)	1.24
(33.55, 14.32, 0.47)	(33.55, 15, 0)	1.23
(34.21, 14.31, 0.47)	(34.21, 15, 0)	1.22
(34.87, 14.29, 0.47)	(34.87, 15, 0)	1.2
(35.53, 14.28, 0.47)	(35.53, 15, 0)	1.19
(36.18, 14.27, 0.47)	(36.18, 15, 0)	1.18
(36.84, 14.26, 0.47)	(36.84, 15, 0)	1.17
(37.5, 14.24, 0.47)	(37.5, 15, 0)	1.16
(38.16, 14.23, 0.47)	(38.16, 15, 0)	1.14
(38.82, 14.22, 0.47)	(38.82, 15, 0)	1.13
(39.47, 14.2, 0.47)	(39.47, 15, 0)	1.12
(40.13, 14.19, 0.47)	(40.13, 15, 0)	1.11
(40.79, 14.18, 0.47)	(40.79, 15, 0)	1.1
(41.45, 14.16, 0.47)	(41.45, 15, 0)	1.08
(42.11, 14.15, 0.47)	(42.11, 15, 0)	1.07
(42.76, 14.14, 0.47)	(42.76, 15, 0)	1.06
(43.42, 14.12, 0.47)	(43.42, 15, 0)	1.05
(44.08, 14.11, 0.47)	(44.08, 15, 0)	1.04
(44.74, 14.1, 0.46)	(44.74, 15, 0)	1.03
(45.39, 14.08, 0.46)	(45.39, 15, 0)	1.02

Table A3. *Cont.*

Abnormal Wear III Rubber Roller Point Cloud Profile Coordinates	Point Cloud Contour Coordinates of Unworn Roller	Euclidean Distance for the Corresponding Coordinates
(46.05, 14.07, 0.46)	(46.05, 15, 0)	1
(46.71, 14.06, 0.46)	(46.71, 15, 0)	0.99
(47.37, 14.05, 0.46)	(47.37, 15, 0)	0.98
(48.03, 14.03, 0.46)	(48.03, 15, 0)	0.97
(48.68, 14.02, 0.46)	(48.68, 15, 0)	0.96
(49.34, 14.01, 0.46)	(49.34, 15, 0)	0.95
(50, 13.99, 0.46)	(50, 15, 0)	0.94
(50.66, 13.98, 0.46)	(50.66, 15, 0)	0.92
(51.32, 13.97, 0.46)	(51.32, 15, 0)	0.91
(51.97, 13.95, 0.46)	(51.97, 15, 0)	0.9
(52.63, 13.94, 0.46)	(52.63, 15, 0)	0.89
(53.29, 13.93, 0.46)	(53.29, 15, 0)	0.88
(53.95, 13.91, 0.46)	(53.95, 15, 0)	0.87
(54.61, 13.9, 0.46)	(54.61, 15, 0)	0.86
(55.26, 13.89, 0.46)	(55.26, 15, 0)	0.85
(55.92, 13.87, 0.46)	(55.92, 15, 0)	0.84
(56.58, 13.86, 0.46)	(56.58, 15, 0)	0.83
(57.24, 13.85, 0.46)	(57.24, 15, 0)	0.82
(57.89, 13.83, 0.46)	(57.89, 15, 0)	0.81
(58.55, 13.82, 0.46)	(58.55, 15, 0)	0.8
(59.21, 13.81, 0.46)	(59.21, 15, 0)	0.79
(59.87, 13.8, 0.45)	(59.87, 15, 0)	0.78
(60.53, 13.78, 0.45)	(60.53, 15, 0)	0.77
(61.18, 13.77, 0.45)	(61.18, 15, 0)	0.76
(61.84, 13.76, 0.45)	(61.84, 15, 0)	0.75
(62.5, 13.74, 0.45)	(62.5, 15, 0)	0.74
(63.16, 13.73, 0.45)	(63.16, 15, 0)	0.73
(63.82, 13.72, 0.45)	(63.82, 15, 0)	0.72
(64.47, 13.7, 0.45)	(64.47, 15, 0)	0.71
(65.13, 13.69, 0.45)	(65.13, 15, 0)	0.7
(65.79, 13.68, 0.45)	(65.79, 15, 0)	0.69
(66.45, 13.66, 0.45)	(66.45, 15, 0)	0.68
(67.11, 13.65, 0.45)	(67.11, 15, 0)	0.67
(67.76, 13.64, 0.45)	(67.76, 15, 0)	0.66
(68.42, 13.62, 0.45)	(68.42, 15, 0)	0.65
(69.08, 13.61, 0.45)	(69.08, 15, 0)	0.64
(69.74, 13.6, 0.45)	(69.74, 15, 0)	0.64
(70.39, 13.58, 0.45)	(70.39, 15, 0)	0.63
(71.05, 13.57, 0.45)	(71.05, 15, 0)	0.62
(71.71, 13.56, 0.45)	(71.71, 15, 0)	0.61
(72.37, 13.55, 0.45)	(72.37, 15, 0)	0.6
(73.03, 13.53, 0.45)	(73.03, 15, 0)	0.6
(73.68, 13.52, 0.45)	(73.68, 15, 0)	0.59
(74.34, 13.51, 0.45)	(74.34, 15, 0)	0.58
(75, 13.49, 0.44)	(75, 15, 0)	0.58
(75.66, 13.48, 0.44)	(75.66, 15, 0)	0.57
(76.32, 13.47, 0.44)	(76.32, 15, 0)	0.56
(76.97, 13.45, 0.44)	(76.97, 15, 0)	0.56
(77.63, 13.44, 0.44)	(77.63, 15, 0)	0.55
(78.29, 13.43, 0.44)	(78.29, 15, 0)	0.54
(78.95, 13.41, 0.44)	(78.95, 15, 0)	0.54
(79.61, 13.4, 0.44)	(79.61, 15, 0)	0.53

Table A4. Numerical simulation data for normal wear roller spacing.

Passthrough Filtering Range	Number of Movable Roller Point Clouds	Number of Fixed Roller Point Clouds
$40 < x_i < 40.5$	137	137
$40.5 < x_i < 41.5$	137	137
$41.5 < x_i < 42$	137	137
$42 < x_i < 42.5$	137	137
$42.5 < x_i < 43.5$	137	137
$43.5 < x_i < 44$	137	137
$44 < x_i < 44.5$	137	137
$44.5 < x_i < 45.5$	137	137
$45.5 < x_i < 46$	137	137
$46.5 < x_i < 47$	137	137
$47 < x_i < 48$	137	137
$47 < x_i < 48$	137	137
$47 < x_i < 48$	137	137
$48 < x_i < 48.5$	137	137
$48.5 < x_i < 49$	137	137
$49 < x_i < 49.5$	137	137
$49.5 < x_i < 50.5$	137	137
$50.5 < x_i < 51$	137	137
$51 < x_i < 51.5$	137	137
$51.5 < x_i < 52.5$	137	137
$52.5 < x_i < 53$	137	137
$53 < x_i < 53.5$	137	137
$53.5 < x_i < 54.5$	137	137
$54.5 < x_i < 55$	137	137
$55 < x_i < 55.5$	137	137
$55.5 < x_i < 56$	137	137
$56 < x_i < 57$	137	137
$57 < x_i < 57.5$	137	137
$57.5 < x_i < 58.5$	137	137
$58.5 < x_i < 59$	137	137
$59 < x_i < 60$	137	137
$60 < x_i < 60.5$	137	137
$60.5 < x_i < 61$	137	137
$61 < x_i < 62$	137	137
$62 < x_i < 62.5$	137	137
$62.5 < x_i < 63$	137	137
$63 < x_i < 64$	137	137
$64 < x_i < 64.5$	137	137
$64.5 < x_i < 65$	137	137
$65 < x_i < 65.5$	137	137

Table A5. Numerical simulation data for roller spacing in abnormal wear I of rubber roller.

Passthrough Filtering Range	Number of Movable Roller Point Clouds	Number of Fixed Roller Point Clouds
$42 < x_i < 43$	143	143
$43 < x_i < 43.5$	143	143
$43.5 < x_i < 44$	143	143
$44 < x_i < 44.5$	143	143
$44.5 < x_i < 45.5$	143	143
$45.5 < x_i < 46$	143	143
$46 < x_i < 46.5$	143	143
$46.5 < x_i < 47$	143	143
$47.5 < x_i < 48.5$	143	143
$48.5 < x_i < 49$	143	143
$49.5 < x_i < 50.5$	143	143

Table A5. *Cont.*

Passthrough Filtering Range	Number of Movable Roller Point Clouds	Number of Fixed Roller Point Clouds
$50.5 < x_i < 51$	143	143
$51 < x_i < 51.5$	143	143
$51.5 < x_i < 52$	143	143
$52 < x_i < 53$	143	143
$53 < x_i < 53.5$	143	143
$53.5 < x_i < 54$	143	143
$54 < x_i < 54.5$	143	143
$54.5 < x_i < 55.5$	143	143
$55.5 < x_i < 56$	143	143
$56 < x_i < 56.5$	143	143
$56.5 < x_i < 57$	143	143
$57 < x_i < 58$	143	143

Table A6. Numerical simulation data for roller spacing in abnormal wear II of rubber roller.

Passthrough Filtering Range	Number of Movable Roller Point Clouds	Number of Fixed Roller Point Clouds
$40 < x_i < 40.5$	150	150
$40.5 < x_i < 41$	150	150
$41 < x_i < 42$	150	150
$42 < x_i < 42.5$	150	150
$42.5 < x_i < 43$	150	150
$43 < x_i < 43.5$	150	150
$43.5 < x_i < 44.5$	150	150
$44.5 < x_i < 45$	150	150
$45 < x_i < 45.5$	150	150
$45.5 < x_i < 46.5$	150	150
$46.5 < x_i < 47$	150	150
$47 < x_i < 47.5$	150	150
$47.5 < x_i < 48.5$	150	150
$48.5 < x_i < 49$	150	150
$49 < x_i < 49.5$	150	150
$49.5 < x_i < 50.5$	150	150
$50.5 < x_i < 51$	150	150
$51 < x_i < 51.5$	150	150
$51.5 < x_i < 52.5$	150	150
$52.5 < x_i < 53$	150	150
$53 < x_i < 53.5$	150	150
$53.5 < x_i < 54.5$	150	150
$54.5 < x_i < 55$	150	150
$55 < x_i < 55.5$	150	150
$55.5 < x_i < 56.5$	150	150
$56.5 < x_i < 57$	150	150
$57.5 < x_i < 57.5$	150	150
$57.5 < x_i < 58.5$	150	150
$58.5 < x_i < 59$	150	150
$59 < x_i < 59.5$	150	150
$59.5 < x_i < 60.5$	150	150
$60.5 < x_i < 61$	150	150
$61 < x_i < 61.5$	150	150
$61.5 < x_i < 62.5$	150	150
$62.5 < x_i < 63$	150	150
$63 < x_i < 63.5$	150	150
$63.5 < x_i < 64.5$	150	150
$64.5 < x_i < 65$	150	150
$65 < x_i < 65.5$	150	150

Table A7. Numerical simulation data for roller spacing in abnormal wear III of rubber roller.

Passthrough Filtering Range	Number of Movable Roller Point Clouds	Number of Fixed Roller Point Clouds
$40 < x_i < 40.5$	137	137
$40.5 < x_i < 41.5$	137	137
$41.5 < x_i < 42$	137	137
$42 < x_i < 42.5$	137	137
$42.5 < x_i < 43.5$	137	137
$43.5 < x_i < 44$	137	137
$44 < x_i < 44.5$	137	137
$44.5 < x_i < 45.5$	137	137
$45.5 < x_i < 46$	137	137
$46 < x_i < 46.5$	137	137
$46.5 < x_i < 47$	137	137
$47 < x_i < 48$	137	137
$48 < x_i < 48.5$	137	137
$48.5 < x_i < 49$	137	137
$49 < x_i < 49.5$	137	137
$49.5 < x_i < 50.5$	137	137

References

1. Bodie, A.R.; Micciche, A.C.; Atungulu, G.G.; Rothrock, M.J., Jr.; Ricke, S.C. Current trends of rice milling byproducts for agricultural applications and alternative food production systems. *Front. Sustain. Food Syst.* **2019**, *3*, 47. [CrossRef]
2. Yang, L.; Fan, Y.; Yin, C.; Wang, C.; Liu, X.; Song, S.; Zhang, Y. Compression and shear fracture behavior of single rice paddy under effect of husking operation. *J. Cereal Sci.* **2022**, *107*, 103538. [CrossRef]
3. Chen, P.; Jia, F.; Zhang, J.; Han, Y.; Li, A.; Wang, Y.; Fei, J.; Shen, S.; Feng, W.; Hao, X. Breakage mechanism of brown rice grain during rubber roll hulling. *Biosyst. Eng.* **2023**, *225*, 41–53.
4. Yang, L.; Fan, Y.; Song, S.; Wang, D.; Zhang, Y.; Cao, M. Frictional behavior of brown rice grain during moderate processing. *Tribol. Int.* **2021**, *162*, 107123.
5. Lieberwirth, H.; Silbermann, F.; Szczelina, P. New insights into double roll crushing. *Miner. Eng.* **2023**, *202*, 108298.
6. Zareiforoush, H.; Komarizadeh, M.; Alizadeh, M. Effects of crop-machine variables on paddy grain damage during handling with an inclined screw auger. *Biosyst. Eng.* **2010**, *106*, 234–242.
7. Jelali, M. Performance assessment of control systems in rolling mills–application to strip thickness and flatness control. *J. Process Control.* **2007**, *17*, 805–816.
8. Rani, A.; Ortiz-Arroyo, D.; Durdevic, P. Advancements in Point Cloud-Based 3D Defect Detection and Classification for Industrial Systems: A Comprehensive Survey. *arXiv* **2024**, arXiv:2402.12923.
9. Ntoulmperis, M.; Catti, P.; Discepolo, S.; van de Kamp, W.; Castellini, P.; Nikolakis, N.; Alexopoulos, K. 3D point cloud analysis for surface quality inspection: A steel parts use case. *Procedia CIRP* **2024**, *122*, 509–514.
10. Zhang, Y.; Fang, C.; Huang, G.; Xu, X. Modeling and simulation of the distribution of undeformed chip thicknesses in surface grinding. *Int. J. Mach. Tools Manuf.* **2018**, *127*, 14–27.
11. Jiang, J.; Ge, P.; Bi, W.; Zhang, L.; Wang, D.; Zhang, Y. 2D/3D ground surface topography modeling considering dressing and wear effects in grinding process. *Int. J. Mach. Tools Manuf.* **2013**, *74*, 29–40. [CrossRef]
12. Kim, M.; Oh, D.; Kim, Y.; Kim, T.; Kim, J. Printing Pressure Uniformization of Roll-to-Roll Process Using Roll Configuration Matching. In Proceedings of the Information Storage and Processing Systems, San Francisco, CA, USA, 29–30 August 2017; p. V001T008A003.
13. Krok, A.; Peciar, M.; Fekete, R. Using the DPIV optical technique to measure the velocity of powder material in the space between the rollers in a roll compactor. *Powder Technol.* **2014**, *262*, 131–141. [CrossRef]
14. Byon, S.; Park, H.; Lee, Y. Experimental study for roll gap adjustment due to roll wear in single-stand rolling and multi-stand rolling test. *J. Mech. Sci. Technol.* **2008**, *22*, 937–945. [CrossRef]
15. Hu, Y.; Sun, J.; Peng, W.; Zhang, D. A novel forecast model based on CF-PSO-SVM approach for predicting the roll gap in acceleration and deceleration process. *Eng. Comput.* **2021**, *38*, 1117–1133. [CrossRef]
16. Guo, Y.; Wang, Y.; Liu, X. Real-time optical detection system for monitoring roller condition with automatic error compensation. *Opt. Lasers Eng.* **2014**, *53*, 69–78. [CrossRef]
17. Liang, Y.-X.; Cao, G.-Z.; Qiu, H.; Huang, S.-D.; Zhou, S.-Q. Development of the three-dimensional scanning system based on monocular vision. In Proceedings of the 2015 6th International Conference on Power Electronics Systems and Applications (PESA), Hong Kong, China, 15–17 December 2015; pp. 1–5.
18. Zhang, Y.; Wang, Y.; Liu, Y.; Lv, D.; Fu, X.; Zhang, Y.; Li, J. A concentricity measurement method for large forgings based on laser ranging principle. *Measurement* **2019**, *147*, 106838. [CrossRef]

19. Ma, H.; Luo, Y.; He, Y.; Pan, S.; Ren, L.; Shang, J. The short-range, high-accuracy compact pulsed laser ranging system. *Sensors* **2022**, *22*, 2146. [CrossRef]
20. Li, J.; Pu, T. Monolithically Integrated Multi-section Semiconductor Lasers: Toward the Future of Integrated Microwave Photonics. In *Optical Imaging and Sensing: Materials, Devices and Applications*; Wiley: Hoboken, NJ, USA, 2023; pp. 215–270.
21. Chen, S.; Zhang, H.; Jin, F.; Wang, L.; Zhao, C. Research on echo characteristics in remote detection with the pulse LiDAR of aerial targets under diverse atmospheric conditions. *Heliyon* **2023**, *9*, e16728. [CrossRef]
22. Suh, Y.S. Laser sensors for displacement, distance and position. *Sensors* **2019**, *19*, 1924. [CrossRef]
23. Chen, S.; Wang, J.; Pan, W.; Gao, S.; Wang, M.; Lu, X. Towards uniform point distribution in feature-preserving point cloud filtering. *Comput. Vis. Media* **2023**, *9*, 249–263. [CrossRef]
24. Chung, Y.-C.; Su, I.-F.; Lee, C.; Liu, P.-C. Multiple k nearest neighbor search. *World Wide Web* **2017**, *20*, 371–398. [CrossRef]
25. Shao, W.J.; Huang, Y.; Zhang, Y. A novel weld seam detection method for space weld seam of narrow butt joint in laser welding. *Opt. Laser Technol.* **2018**, *99*, 39–51. [CrossRef]
26. Zhang, G.; Liu, Z.; Sun, J.; Wei, Z. Novel calibration method for a multi-sensor visual measurement system based on structured light. *Opt. Eng.* **2010**, *49*, 043602. [CrossRef]
27. Han, Y.; Jia, F.; Zeng, Y.; Jiang, L.; Zhang, Y.; Cao, B. Effects of rotation speed and outlet opening on particle flow in a vertical rice mill. *Powder Technol.* **2016**, *297*, 153–164. [CrossRef]
28. Zhang, J.; Spikes, H. Measurement of EHD friction at very high contact pressures. *Tribol. Lett.* **2020**, *68*, 42. [CrossRef]
29. Shen, G.; Yu, C.; Ren, Z.; Xing, J.; Xiao, H. Mechanism generating deviations in the rolling load and strip camber on the plate rolling mill. *Ironmak. Steelmak.* **2017**, *44*, 707–711. [CrossRef]
30. Fischler, M.A.; Bolles, R.C. Random sample consensus: A paradigm for model fitting with applications to image analysis and automated cartography. *Commun. ACM* **1981**, *24*, 381–395. [CrossRef]
31. Xu, B.; Jiang, W.; Shan, J.; Zhang, J.; Li, L. Investigation on the weighted ransac approaches for building roof plane segmentation from lidar point clouds. *Remote Sens.* **2015**, *8*, 5. [CrossRef]
32. Kluger, F.; Brachmann, E.; Yang, M.Y.; Rosenhahn, B. Robust Shape Fitting for 3D Scene Abstraction. *IEEE Trans. Pattern Anal. Mach. Intell.* **2024**, *46*, 6306–6325. [CrossRef]
33. Jin, Y.-H.; Lee, W.-H. Fast cylinder shape matching using random sample consensus in large scale point cloud. *Appl. Sci.* **2019**, *9*, 974. [CrossRef]
34. Faghih, S.; Behravesh, S.B.; Shaha, S.K.; Jahed, H. Effect of split sleeve cold expansion on fatigue and fracture of rolled AZ31B magnesium alloy. *Theor. Appl. Fract. Mech.* **2023**, *123*, 103715. [CrossRef]
35. Yang, Y.; Fang, H.; Fang, Y.; Shi, S. Three-dimensional point cloud data subtle feature extraction algorithm for laser scanning measurement of large-scale irregular surface in reverse engineering. *Measurement* **2020**, *151*, 107220. [CrossRef]
36. Minaker, B.; Nantais, N. An eigenvector approach to roll centre analysis. In *SAE Transactions*; SAE International: Warrendale, PA, USA, 2007; pp. 897–901.
37. Lin, S.; Jusko, O.; Härtig, F.; Seewig, J. A least squares algorithm for fitting data points to a circular arc cam. *Measurement* **2017**, *102*, 170–178. [CrossRef]
38. Li, D.; Mei, H.; Shen, Y.; Su, S.; Zhang, W.; Wang, J.; Zu, M.; Chen, W. ECharts: A declarative framework for rapid construction of web-based visualization. *Vis. Inform.* **2018**, *2*, 136–146. [CrossRef]

Disclaimer/Publisher's Note: The statements, opinions and data contained in all publications are solely those of the individual author(s) and contributor(s) and not of MDPI and/or the editor(s). MDPI and/or the editor(s) disclaim responsibility for any injury to people or property resulting from any ideas, methods, instructions or products referred to in the content.